

# Measurement of the Casimir force between superconductors

Matthijs H. J. de Jong,<sup>1</sup> Evren Korkmazgil,<sup>1</sup> Louise Banniard,<sup>1</sup> Mika A. Sillanpää,<sup>1</sup> and Laure Mercier de Lépinay<sup>1,\*</sup>

<sup>1</sup>*Department of Applied Physics, Aalto University, FI-00076 Aalto, Finland*

(Dated: January 15, 2026)

The Casimir force follows from quantum fluctuations of the electromagnetic field and yields a nonlinear attractive force between closely spaced conductive objects. Its magnitude depends on the conductivity of the objects up to optical frequencies. Measuring the Casimir force in superconductors should allow to isolate frequency-specific contributions to the Casimir effect, as frequencies below the superconducting gap energy are expected to contribute differently than those above it. There is significant interest in this contribution as it is suspected to contribute to an unexplained discrepancy between predictions and measurements of the Casimir force between normal metals, which questions the basic principles on which estimates of the magnitude are based. Here, we observe the Casimir force between superconducting objects through the nonlinear dynamics it imparts to a superconducting drum resonator in a microwave optomechanical system. There is excellent agreement between the experiment and the Casimir force magnitude computed for this device across three orders of magnitude of displacement. Furthermore, the Casimir nonlinearity is intense enough that, with a modified design, this device type should operate in the single-phonon nonlinear regime. Accessing this regime has been a long-standing goal that would greatly facilitate quantum operations of mechanical resonators.

## INTRODUCTION

A significant body of theoretical and experimental works over the last 20 years has focused on understanding the Casimir force<sup>1–7</sup>. This is motivated in part by the Casimir effect's practical applications in MEMS<sup>8–13</sup>, but to a larger extent by its intimate connection to heat and energy transfer<sup>14,15</sup>, especially at finite conductivity and temperature<sup>16–19</sup>. Furthermore, Casimir force experiments have also put bounds on Yukawa corrections to short-distance Newtonian gravity<sup>20,21</sup> and the Casimir effect has been proposed as a candidate to account for dark energy in cosmology<sup>22</sup>. Recently, the interplay between the Casimir force and superconductivity has garnered interest, either manifesting as a correction to the superconducting condensation energy<sup>23,24</sup>, or as a correction to the electric permittivity of the material<sup>25–28</sup>, and it could shed light on the discrepancy between the calculated and experimentally observed Casimir force between metals<sup>19,28,29</sup>. While most room-temperature experiments rely on a variation of the distance between objects to observe the expected force-distance scaling<sup>3,4,11,12,30</sup>, it is challenging to perform this type of experiment with superconductors due to the difficulty of precise positioning in cryogenic environments. By contrast, the strong nonlinearity imparted by the Casimir potential can be easily shown through the dynamical behavior without relying on precise positioners. Only few works have studied the Casimir force through the nonlinear dynamics<sup>31,32</sup>.

Strong nonlinearities in oscillators at cryogenic temperatures are especially interesting in the context of resonators in the quantum regime. Cavity optomechanics, where the motion of an object couples to the electromagnetic field of a cavity, has allowed to engineer Gaussian quantum mechanical states in cryogenic mechanical oscillators. The phase-space distribution of these states is Gaussian, similarly to classical states, but with variances lower than thresholds determined

by quantum mechanics. Notably, resonators were cooled to the ground state<sup>33</sup>, their uncertainty was squeezed below the magnitude of quantum fluctuations<sup>34–36</sup>, entangled states of two oscillators were prepared<sup>37,38</sup>, and mechanical states were measured avoiding quantum backaction<sup>39</sup>. However, linear optomechanical systems cannot realize non-Gaussian quantum states such as Fock states, cat states, and entangled combinations thereof, which are desirable for quantum algorithms. To realize these states nonetheless, mechanical oscillators have been addressed with non-Gaussian photonic states<sup>40,41</sup>, or coupled to superconducting qubits<sup>42–45</sup> or quantum dots<sup>46</sup> to inherit their nonlinearity. In contrast, the nonlinearity imparted by the Casimir force to a superconducting drum resonator is intrinsic to the construction of the system; It does not rely on coupling to another system.

In this work, we have observed a nonlinear potential that we show to be quantitatively compatible with the Casimir potential acting between the plates of a type-I superconducting drum. This force yields a strong softening nonlinearity, where the resonating frequency decreases with increasing amplitude<sup>9,31,32</sup>. The optomechanical coupling to a microwave cavity allows us to calibrate all properties of the system and compare its response to that obtained within a model of Casimir potential with only a single fit parameter. We qualitatively and quantitatively exclude other (nonlinear) effects that have hindered earlier works<sup>26,30,47</sup>. This system requires no cryogenic positioners, and it shows a strong, tunable mechanical nonlinearity that is fully compatible with a mechanical system where quantum operations have been achieved.

## RESULTS

### The Casimir nonlinearity

The drum resonator consists of two plates made of evaporated aluminium, where the minimum of the harmonic mechanical potential would correspond to a vacuum gap of  $d = 18.00 \pm 0.25$  nm at cryogenic temperatures. This very narrow

\* laure.mercierdelepinay@aalto.fi

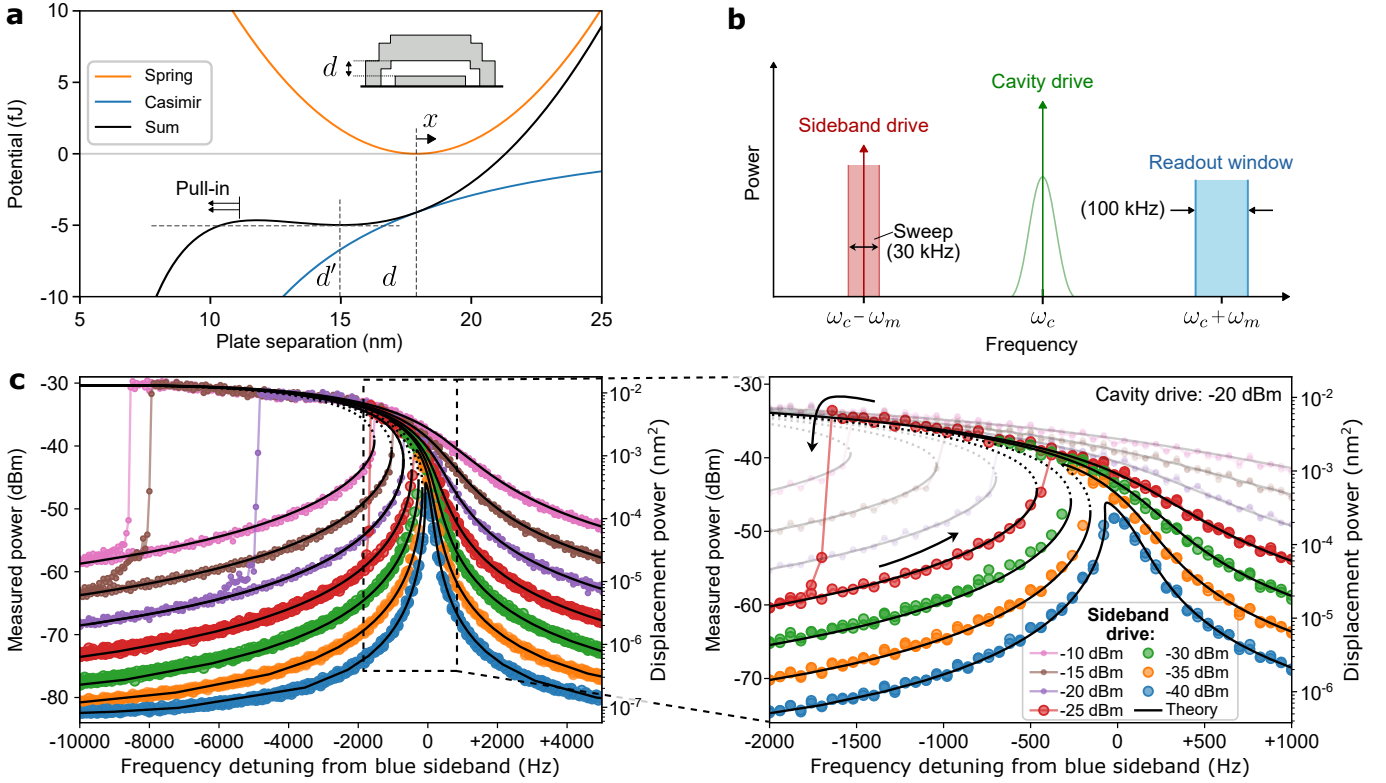


**Fig. 1 | Effects of a Casimir force on a superconducting drum resonator.** **a:** Our device consists of two plates separated by a vacuum gap. The top plate is mechanically compliant and experiences a mechanical restoring potential (orange line) which is minimum for a separation  $d$  between plates (see inset). The Casimir potential (blue) adds to this restoring potential, and the sum (black) has a local minimum at separation  $d'$  shifted from  $d$ . The total potential is not harmonic around  $d'$  for large amplitudes which causes nonlinear behavior. **b:** Schematic of the microwave optomechanical measurement scheme. We strongly drive the microwave cavity at its center frequency, with an additional strong drive tone at  $\omega_{sb}$  which is close to  $\omega_c - \omega_m$ . The sideband drive is swept in frequency, and we read out the emitted signal in a window around  $\omega_c + \omega_m$ . **c:** Measured displacement response for various nominal sideband drive powers (labels) at  $-20$  dBm cavity drive, showing the expected Lorentzian behavior at low drive power that transitions to a strong softening nonlinearity at high drive power. The Casimir force solution (black line) becomes multi-valued, with two stable branches (solid black) and an unstable solution (dotted black/semitransparent). Our measurements follow the stable solutions, leading to a hysteresis depending on the sweep direction. The theory matches well to all curves using only a single fit parameter,  $d$ , common to all curves. The right panel highlights details of the center region indicated by the dashed box, and the hysteresis depending on the sweep direction is indicated by arrows. The data points at the highest powers are made transparent for visual clarity.

vacuum gap implies a strong Casimir effect, so the Casimir force draws the mechanically compliant top plate closer to the bottom plate that is fixed to a rigid substrate. The shift of the rest position of the top plate is significant: The equilibrium position with the Casimir force taken into account – which is the real physical situation – corresponds to a vacuum gap  $d' = d - 2.9 \text{ nm} = 15.1 \text{ nm}$ , which we schematically show in Fig. 1a. Without the Casimir effect, the top plate would oscillate with unperturbed frequency  $\omega_r$  (see Table 1) around the minimum of elastic potential energy at a distance  $d$  from the bottom plate's top surface. But due to the Casimir force, it oscillates with frequency  $\omega_m$  around the local minimum of the total potential at separation  $d'$  (the equilibrium position). It can stably oscillate around this local minimum with a small amplitude, but at larger amplitudes the frequency decreases (spring softening) until it reaches the pull-in point, beyond which the top plate will collapse onto the bottom plate<sup>8,27</sup>. We

model the dynamics of our system as

$$\ddot{x} + \gamma_r \dot{x} + \omega_r^2 x + \frac{P}{(x+d)^n} \frac{\pi r^2}{m_{\text{eff}}} = \frac{F_0}{m_{\text{eff}}}, \quad (1)$$

which describes the evolution of a point-like harmonic oscillator in one dimension with displacement coordinate  $x$ , resonance frequency  $\omega_r$ , effective mass  $m_{\text{eff}}$ , and decay rate  $\gamma_r$  driven by a force  $F_0$ . We note that this model reducing the distributed motion of the membrane to a scalar coordinate with an effective mass stays roughly valid in presence of a nonlinear potential. It is additionally subject to a force derived from the Casimir pressure, the last term on the left-hand side, that works on the area of the drum,  $\pi r^2$ . We compute the Casimir pressure for the real material based on the Mattis-Bardeen conductivity for (BCS) superconductors<sup>28</sup>, see Methods. We fit the Casimir pressure to an expression of the form  $P_c = \frac{P}{(x+d)^n}$  where  $P \simeq 1275 \cdot 10^{-24} \text{ Pa} \cdot \text{m}^n$  and pressure-distance scaling  $n = 3.193$ . The Casimir pressure experienced by the

| Quantity                          | Symbol                      | Value   |
|-----------------------------------|-----------------------------|---|
| Unperturbed frequency             | $\omega_r$                  | $2\pi \times 16.247$ MHz                        |
| Mechanical frequency              | $\omega_m$                  | $2\pi \times 10.001$ MHz                        |
| Mechanical linewidth              | $\gamma_r \approx \gamma_m$ | $2\pi \times 168.9 \pm 9.5$ Hz                  |
| Cavity frequency                  | $\omega_c$                  | $2\pi \times 5.461831$ GHz                      |
| External linewidth                | $\kappa_e$                  | $2\pi \times 250.8 \pm 2.1$ kHz                 |
| Internal linewidth                | $\kappa_i$                  | $2\pi \times 297.2 \pm 2.8$ kHz                 |
| Drive frequency                   | $\omega_{mw}$               | $\approx \omega_c$                              |
| Sideband frequency                | $\omega_{sb}$               | $\approx \omega_{mw} - \omega_m$                |
| Detuning $\omega_c - \omega_{mw}$ | $\Delta$                    | $<  2\pi \times 1 $ kHz                         |
| Optomechanical coupling           | $g_0$                       | $2\pi \times 150 \pm 9$ Hz                      |
| Effective mass                    | $m_{eff}$                   | $3.96 \times 10^{-14}$ kg                       |
| Rest separation without Cas. f.   | $d$                         | $18.00 \pm 0.25$ nm                             |
| Rest separation                   | $d'$                        | $15.10 \pm 0.25$ nm                             |
| Bottom plate diameter             | $2r$                        | $11.3$ $\mu$ m                                  |
| Moving plate diameter             | -                           | $14.5$ $\mu$ m                                  |
| Casimir pressure at equilibrium   | $P_c$                       | $12.0 \pm 0.6$ kPa                              |
| Casimir amplitude                 | $P$                         | $(1275 \pm 7) \cdot 10^{-24}$ Pa m <sup>n</sup> |
| Casimir force scaling exponent    | $n$                         | 3.193   |

**Table 1 | The parameters of our system.** The parameters are either fitted (with 95% confidence interval) and from theory or design.

drum at its equilibrium position  $d' = 15.10 \pm 0.25$  nm (corresponding to the value  $x \approx -2.9$  nm) is  $P_c \approx 12.0 \pm 0.6$  kPa.

The drum resonator is mounted in a dilution cryostat and stabilized at 10 mK (see [Methods](#)), so the aluminium is deep in the superconducting regime. The drum forms the variable capacitance of a microwave cavity, which we drive with two strong drives, one at the resonance frequency of the microwave cavity,  $\omega_c$  (cavity drive), and the other at the red sideband  $\omega_c - \omega_m$  (sideband drive) as shown schematically in [Fig. 1b](#). This combination of tones generates a driving force on the mechanical resonator such that the mechanical amplitude scales linearly with either drive power (see [Supplementary Sec. A](#)). All drive powers are reported as their nominal values at room temperature, they are divided by attenuators before reaching the sample as shown in [Methods](#). The cavity drive power is much larger than the sideband drive, and we sweep the frequency of the weaker sideband drive within a range of 30 kHz both upwards and downwards in frequency. We record the output signal of the cavity with a spectrum analyzer in a 100 kHz window centered around  $\omega_c + \omega_m$  (blue sideband).

The signal we observe at the readout sideband is proportional to the displacement of the resonator. At low drive powers, we see a Lorentzian response, but increasing the cavity drive power in [Fig. 1c](#) shows the strong softening nonlinearity expected of the Casimir force<sup>9</sup>. At high drive powers, this nonlinearity creates two stable solutions to [Eq. \(1\)](#) over a limited range of frequencies (a low-amplitude and a high-amplitude branch) with an unstable solution in between. The sweep direction determines which branch is followed as indicated by arrows in [Fig. 1c](#). The resonator amplitude jumps up at the end of the low-amplitude branch (bifurcation point), but it jumps down from the high-amplitude branch at a point before the end of the branch. This occurs due to our stepped sweep protocol (see [Methods](#)).

We compute the expected displacement of the oscillator of

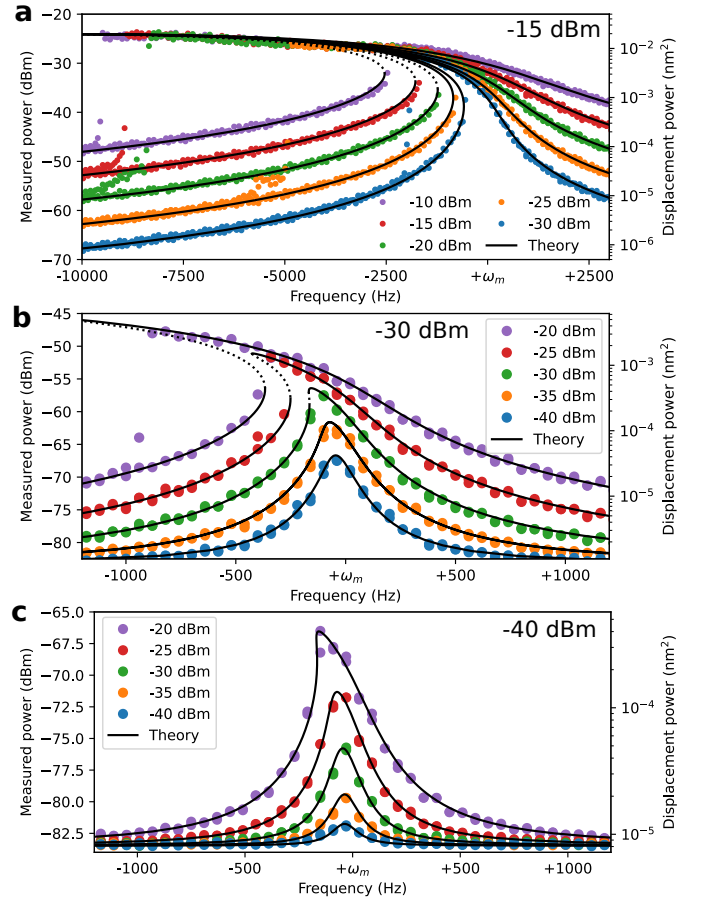


**Fig. 2 | Responses measured for all combinations of drive parameters for cavity drive powers (a:  $-15$  dBm, b:  $-30$  dBm, c:  $-40$  dBm) and sideband drive powers (colors). All theory curves (black lines) across all panels share only a single fit parameter  $d$ .**

[Eq. \(1\)](#) for a frequency-swept drive (see [Methods](#) and [Supplementary Information](#)) using the parameters of [Table 1](#). The resulting curves are plotted as black lines in [Fig. 1c](#), with the unstable part of the solution as a dotted line. All curves collectively share a single fit parameter,  $d$ , and show excellent agreement with the measured signal. We repeat the experiment at different combinations of cavity and sideband drive powers, shown in [Fig. 2](#). Our theory model accurately describes the shape of the signal across more than three orders of magnitude in displacement, up to a maximum measured amplitude of  $\approx 100$  pm. This provides strong indication of a successful measurement of the Casimir force between superconducting plates.

### Calibration of displacement amplitude

To make  $d$  (the vacuum gap at the minimum of the harmonic mechanical potential) the only fit parameter, we calibrate all other parameters listed in [Table 1](#) to accurately infer the displacement amplitude of the resonator. The drum resonator is embedded in an optomechanical cavity such that

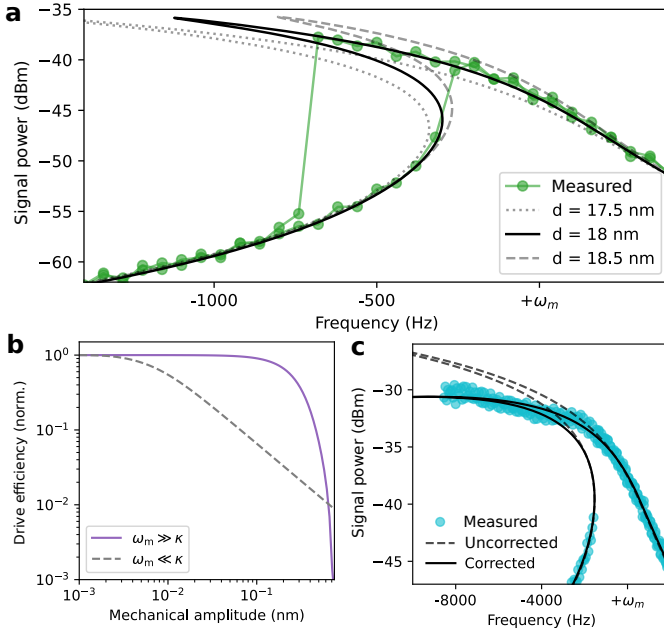


**Fig. 3 | Optomechanical calibration.** **a:** Theory curves generated with equal maximum mechanical amplitude for various values of  $d$  (black & grey lines). For smaller  $d$ , the Casimir force is stronger and leads to a larger softening nonlinearity. For  $d = 18$  nm there is excellent agreement with the measured data (green). **b:** The drive efficiency decreases sharply from 1 at high amplitude, as most of the time the instantaneous cavity frequency  $\omega_c(t)$  is far away from the drive frequency. This effect is stronger, comparatively, in the bad cavity limit ( $\omega_m \ll \kappa$ ), but it is noticeable in our experiments at the largest amplitudes. **c:** The drive efficiency leads to a correction in the Casimir curves at large amplitudes.

its position couples to the radiation pressure, resulting in the equations of motion<sup>48</sup>,

$$\begin{aligned}\hat{\dot{x}}(t) &= \omega_m \hat{p}, \\ \hat{\dot{p}}(t) &= -\omega_m \hat{x} - \gamma_m \hat{p} - g_0 \hat{a}^\dagger \hat{a} + \sqrt{\gamma_m} \hat{\xi}(t), \\ \hat{\dot{a}}(t) &= -(i\Delta + \kappa/2) \hat{a} + ig_0 \hat{x} \hat{a} + \sqrt{\kappa_e} \hat{s}_{in}(t) + \sqrt{\kappa} \hat{a}_{noise}(t).\end{aligned}\quad (2)$$

Here, we use operators  $\hat{x}$  and  $\hat{p}$  for position and momentum, and  $\hat{a}$  for the cavity field. We work in a frame rotating at the frequency of the cavity drive, which is detuned by  $\Delta$  from the cavity resonance frequency. The cavity linewidth  $\kappa = \kappa_e + \kappa_i$  is the sum of the external and internal decay rates (see Table 1). The optomechanical single-photon coupling is  $g_0$ . Both operators for the mechanical noise  $\hat{\xi}(t)$  and cavity noise  $\hat{a}_{noise}$ , and an operator for the input signal  $\hat{s}_{in}$  complete the standard dispersive single-mode optomechanical system.

The equations of motion, Eq. (2), depend on parameters  $\omega_m$ ,  $\gamma_m$ ,  $g_0$ ,  $\kappa$ , and  $\Delta$ . We calibrate cavity parameters  $\kappa_e$  and  $\kappa_i$  from the microwave response, and get the single-photon coupling  $g_0$  and the power at our detector from a given displacement power from the amplitude of thermal motion of the drum resonator at 10 mK (see the [Supplementary Information](#)). With the calibrated optomechanical parameters, we obtain the large-amplitude classical response from Eq. (2) for all combinations of power in the cavity drive and red sideband

drive. We compare the predicted relative powers in two sidebands (red and blue), and the off-resonant (directly reflected) red sideband drive with our experimentally observed powers. The relative powers in the sidebands are unaffected by attenuation or amplification on the input and output lines. We get excellent agreement for all combinations of drive powers using the calibrated optomechanical parameters, as shown in the [Supplementary Information](#). The value of the drive force  $F_0$  in the model of Eq. (1) is then inferred as the value that generates the experimentally measured displacement.

Parameters  $P$  and  $n$  are related to material parameters, which are accurately known for Aluminium (see [Methods](#)), so we take them as fixed values. This makes  $d$  the sole fit parameter to compare the solution of Eq. (2) to our experimental observations. In Fig. 3a, we show that  $d = 18$  nm generates the best-fitting solution. Also solutions with  $d = 17.5$ , 18, and 18.5 nm are overlaid on experimental data obtained at  $-20$  dBm cavity drive and  $-30$  dBm sideband drive. The fit procedure is applied to all measured response signals (see Fig. 2). From this collective fit, we estimate the uncertainty of  $d$  as the upper bound of the uncertainty propagated from the amplitude calibration and the standard error of the fitted response signal. The uncertainty we find this way is larger than the uncertainty in  $d$  we would have found from variations in parameters  $P$  and  $n$ , which motivates our choice to treat them as fixed values.

### Drive efficiency

At the core of Eq. (2) is the notion that the cavity frequency depends on the mechanical position,  $\omega_c(x)$ . For a large enough displacement amplitude  $x$ , the cavity frequency shifts by more than the cavity linewidth  $\kappa$  such that the cavity drive tone is mostly reflected. This reduces the amount of circulating power in the cavity, and it reduces the effectiveness of the drive on the mechanical resonator. We estimate this loss of efficiency and compensate for it in the following way. We define the ‘drive efficiency’ as the circulating power in the cavity at some mechanical amplitude normalized to the power at low displacement. It is straightforward to calculate by solving Eq. (2) for fixed amplitude of mechanical motion, and the results are plotted in Fig. 3b. In the experiment  $\omega_m \gg \kappa$  so the drive efficiency is close to 1 up to  $\sim 100$  pm and strongly decreases beyond that.

The effect of the drive efficiency on our Casimir theory is shown in Fig. 3c. For the frequencies where the mechanical amplitude is small, the uncorrected and corrected curves overlap since the drive efficiency is 1. At large amplitudes the uncorrected prediction overestimates the measured response ( $-20$  dBm cavity drive and  $-10$  dBm sideband drive). The correction from the drive efficiency also gives a sanity check on the amplitude calibration, since it originates completely from Eq. (2), which is independent of the Casimir effect.

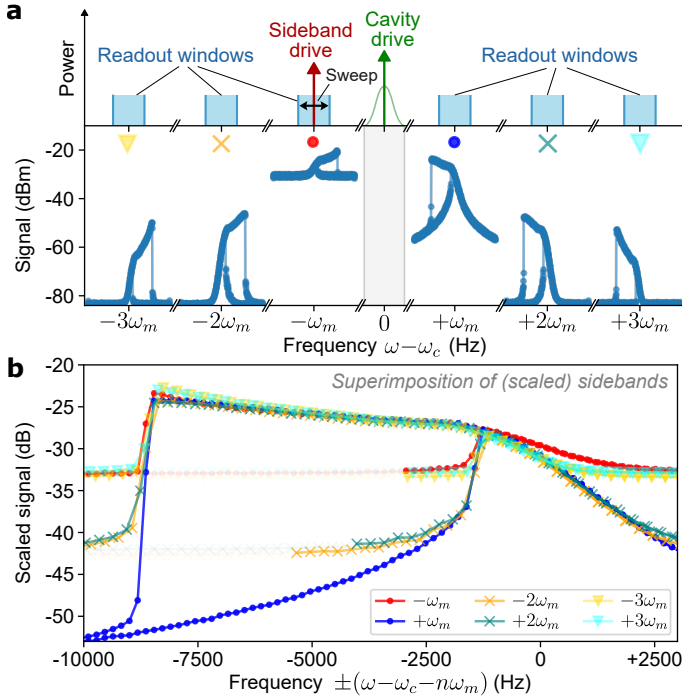


**Fig. 4 | Response observed at higher-order sidebands.** **a:** The full optomechanical measurement consists of six sidebands that are read out sequentially. The first red sideband ( $-\omega_m$ ) is at the same frequency as our swept sideband drive, so its signal is superposed on a pedestal from the directly reflected sideband drive signal. **b:** Superimposition of sidebands. All sidebands encode the mechanical displacement with a known proportionality (see main text), so they collapse on top one another when overlaid. The frequency axis of each sideband has been shifted to align the sideband frequencies  $\omega_c + n\omega_m$ , and the frequency axis of the red sidebands (below the cavity frequency) has been flipped about the sideband frequency. Furthermore the frequency range has been divided by two for second sidebands and three for third sidebands. The vertical axes of 2<sup>nd</sup> and 3<sup>rd</sup> order sidebands have been squared and cubed respectively, as expected from theory.

### The optomechanical nonlinearity

The optomechanical interaction, Eq. (2), is nonlinear. As a result, at large amplitude the higher-order scattering terms yield multiple equally-spaced peaks in the observed response. We read out six of these sidebands, at  $\omega_c \pm n \times \omega_m$  ( $n = 1, 2, 3$ ), as shown in Fig. 4a. The higher-order sidebands can be viewed as repeated scattering events. We extend classical scattered mode theory<sup>49</sup> to cover all six sidebands. We write the system of linear coupled equations for the classical field amplitudes  $a_n$  at the corresponding frequency components in ma-

trix form,

$$\begin{bmatrix} 1 & d_{+3} & 0 & 0 & 0 & 0 & 0 \\ d_{+2} & 1 & d_{+2} & 0 & 0 & 0 & 0 \\ 0 & d_{+1} & 1 & d_{+1} & 0 & 0 & 0 \\ 0 & 0 & d_0 & 1 & d_0 & 0 & 0 \\ 0 & 0 & 0 & d_{-1} & 1 & d_{-1} & 0 \\ 0 & 0 & 0 & 0 & d_{-2} & 1 & d_{-2} \\ 0 & 0 & 0 & 0 & 0 & d_{-3} & 1 \end{bmatrix} \begin{bmatrix} a_{+3} \\ a_{+2} \\ a_{+1} \\ a_0 \\ a_{-1} \\ a_{-2} \\ a_{-3} \end{bmatrix} = \begin{bmatrix} 0 \\ 0 \\ 0 \\ \frac{a_{mw} \sqrt{\kappa_c}}{-i\Delta + \kappa/2} \\ 0 \\ 0 \\ 0 \end{bmatrix} \quad (3)$$

with

$$d_{\pm n} = \frac{g_0 x_{amp}}{2x_{zpf}} \frac{1}{-i(\Delta \pm n\omega_m) + \kappa/2}. \quad (4)$$

Here  $a_{mw}$  is the input power of the microwave drive at the cavity frequency,  $a_{sb}$  is the input power of the microwave drive at the red sideband. We cut off the scattering processes above order  $|n| = 3$ , retaining 7 frequency ranges in Eq. (3). This is a valid approximation when  $g_0 \ll \kappa/2$ , since each individual photon is much more likely to exit the cavity than to scatter from the mechanical resonator. For more details, see the [Supplementary Information](#). The power in the first-order sidebands ( $\pm\omega_m$ ) scales linearly with the amplitude of mechanical displacement  $x_{amp}$ , while the second order sidebands ( $\pm 2\omega_m$ ) scale quadratically and the third order sidebands ( $\pm 3\omega_m$ ) scale cubically. The span of the sweep is doubled and tripled for the second and third mode. When we combine these known behaviors and flip the frequency of the  $-1, -2, -3 \times \omega_m$  sidebands, we can perfectly overlay all sidebands in the high-amplitude regime (Fig. 4b). This shows that although the higher-order peaks arise from a nonlinear optomechanical effect, the profile of the response is unaffected by the optomechanical nonlinearity. Thus, even at large mechanical amplitudes the cavity output signal gives an accurate account of the mechanical displacement.

## DISCUSSION

There are many other effects that could result in an apparent nonlinearity, such as the electrostatic force between the drum plates, potential patches in the aluminium, the geometric nonlinearity, the nonlinear optomechanical coupling, and superconducting vortices. We can rule out these effects as an alternative explanation for our observations, as described in detail in the [Supplementary Information](#). Put briefly, we estimate the pressure contributed by e.g., potential patches, based on Kelvin probe force measurements of the electrostatic potential. We simulate the effect of patches in our geometry<sup>50</sup>, and find that the patch pressure is several orders of magnitude smaller than the Casimir pressure at our plate separation. Based on this, we rule out the effect of potential patches (and similar for the other effects described in the [Supplementary Information](#)). To the best of our knowledge, there are no other sources of nonlinearity that could mimic the Casimir force in both amplitude and scaling.

Our future experiments will involve a gate electrode patterned around the drum plate to allow electrostatic tuning of

the separation<sup>30</sup> and, by extension, the Casimir force. A modest 100 Pa electrostatic pressure is achievable, and sufficient to merge the locally stable solution used in this work with the pull-in point. This should allow the Casimir effect to create nonlinear mechanics on the single-phonon level, a long-standing goal previously only achieved by coupling to external systems<sup>45,46</sup>. The gate electrode will also allow us to improve the accuracy of the amplitude calibration to improve our bounds on  $d$  and  $P_c$ , to shed light on the Casimir puzzle<sup>19</sup> of materials with finite conductivity.

In summary, we have shown the effect of a likely Casimir force between superconducting plates, through its nonlinear nature. We developed a calibration method to translate the power spectrum of a multi-frequency microwave signal into a mechanical amplitude, which leads to an estimate of the Casimir force. With this method we find excellent agreement between our experiment and the computed Casimir force, across three orders of magnitude of mechanical displacement. Due to the exceptionally small spacing, a vacuum gap of 15 nm, our Casimir force is much larger than in conventional Casimir experiments, including those at room temperature. This makes our system well-suited to accurately probe the remaining uncertainties around the Casimir effect. By adding a gate electrode, we could improve the precision of our nonlinear-dynamics-based Casimir measurements be-

yond the small predicted change at the superconducting transition<sup>28</sup>. More fundamentally, the strength of the Casimir effect in our experimental setup gives unique access to an extremely strong, tuneable nonlinearity that is intrinsic to the mechanical system. This means that we could obtain well-separated mechanical energy levels without resorting to the nonlinearity of another system, i.e., bring the mechanical resonator into quantum regime without interactions with non-Gaussian photon states or coupling to an external nonlinear system. Furthermore, the competition between the Casimir potential and the elastic potential can be tuned electrostatically, in situ, to be locally flat, which could be used to probe macroscopic mechanical quantum tunneling<sup>51</sup> or make a mechanical qubit<sup>45,52</sup>.

## METHODS

### Calculation of the Casimir force

To compute the Casimir force between the superconducting plates of our drum, we follow exactly the method of Bimonte<sup>28</sup>. It is based on the Lifshitz formula<sup>2</sup> for the pressure  $P(d, T)$  between two plates as a function of their separation  $d$  and temperature  $T$ ,

$$P(d, T) = \frac{-k_B T}{\pi} \sum_0^\infty \int_0^\infty dk_\perp k_\perp q_\ell \left( \left[ \frac{e^{2dq_\ell}}{r_{\text{TE},1}(i\xi_\ell, k_\perp) r_{\text{TE},2}(i\xi_\ell, k_\perp)} - 1 \right]^{-1} + \left[ \frac{e^{2dq_\ell}}{r_{\text{TM},1}(i\xi_\ell, k_\perp) r_{\text{TM},2}(i\xi_\ell, k_\perp)} - 1 \right]^{-1} \right), \quad (5)$$

where  $k_\perp$  is the in-plane momentum, the  $\ell = 0$  term in the sum has a weight of one half,  $\xi_\ell = 2\pi\ell k_B T / \hbar$  are the imaginary Matsubara frequencies,  $q_\ell = \sqrt{\xi_\ell^2 / c^2 + k_\perp^2}$ , and TE and TM indicate the two independent polarizations of the electromagnetic field. The Fresnel reflection coefficients for the polarizations (TE, TM) and plates (1, 2) are<sup>28</sup>

$$\begin{aligned} r_{\text{TE}}(i\xi_\ell, k_\perp) &= \frac{q_\ell - s_\ell}{q_\ell + s_\ell}, \\ r_{\text{TM}}(i\xi_\ell, k_\perp) &= \frac{\epsilon_\ell q_\ell - s_\ell}{\epsilon_\ell q_\ell + s_\ell}, \end{aligned} \quad (6)$$

where  $s_\ell = \sqrt{\epsilon_\ell \xi_\ell^2 / c^2 + k_\perp^2}$  and electric permittivity  $\epsilon_\ell = \epsilon(i\xi_\ell)$  for the materials of each of the plates 1 and 2. For normal-state materials, we use the Drude model dielectric function  $\epsilon_{\text{Drude}}$ . For superconductors, the Mattis-Bardeen formula gives a corrected function  $\epsilon_{\text{BCS}}$ . The analytic continuation of both functions has been derived as<sup>25,28</sup>

$$\begin{aligned} \epsilon_{\text{Drude}}(i\xi) &= \epsilon_0 + \frac{\Omega_p^2}{\xi(\xi + \gamma_p)}, \\ \epsilon_{\text{BCS}}(i\xi) &= \epsilon_0 + \frac{\Omega_p^2}{\xi} \left( \frac{1}{\xi + \gamma_p} + \frac{g(\xi, T)}{\xi} \right). \end{aligned} \quad (7)$$

Here,  $\Omega_p$  represents the plasma frequency for intraband transitions,  $\gamma_p$  is the relaxation frequency. The contribution from BCS theory is in the form of the factor  $g(\xi, T)$ , given as<sup>28</sup>

$$g(\xi, T) = \int_{-\infty}^{\infty} \frac{d\epsilon}{E} \tanh\left(\frac{E}{2k_B T}\right) \text{Re}[G_+(i\xi, \epsilon)]. \quad (8)$$

This expression is valid for temperatures below the superconducting transition temperature,  $T < T_c$ . The function  $G_+$  is defined as

$$\begin{aligned} G_+(z, \epsilon) &= \frac{\epsilon^2 Q_+(z, E) + [Q_+(z, E) + i\hbar\gamma] A_+(z, E)}{Q_+(z, E) (\epsilon^2 - [Q_+(z, E) + i\hbar\gamma])}, \\ E &= \sqrt{\epsilon^2 + \Delta^2}, \end{aligned} \quad (9)$$

$$\begin{aligned} Q_+(z, E) &= \sqrt{(E + \hbar z)^2 - \Delta^2}, \\ A_+(z, E) &= E(E + \hbar z) + \Delta^2, \end{aligned}$$

and the superconducting gap  $\Delta(T)$  is temperature dependent,

$$\Delta = c_1 k_B T_c \sqrt{1 - \frac{T}{T_c} \left( c_2 + c_3 \frac{T}{T_c} \right)}, \quad (10)$$

where we take  $c_1 = 1.764$ ,  $c_2 = 0.9963$ , and  $c_3 = 0.7735$  from BCS theory<sup>53</sup>.

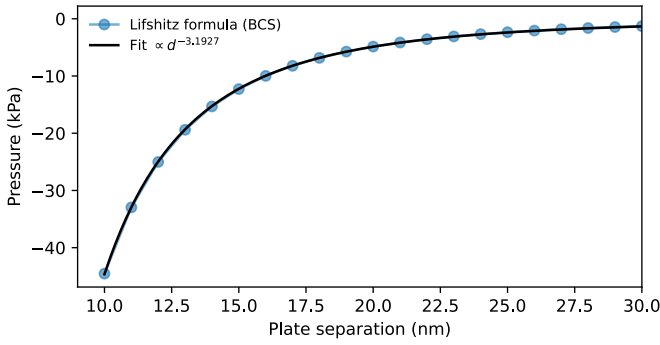


**Fig. 5 | The Casimir pressure.** The Casimir pressure for various distances as calculated via the Lifshitz formula and the BCS model, and a fit proportional to  $d^{-3.193}$ .

To evaluate the expression of Eq. (5), we need the material parameters for aluminium, which are tabulated<sup>54</sup>. We use  $\Omega_p = 13 \text{ eV}/\hbar$ ,  $\gamma_p = \gamma_0/\text{RRR}$  where  $\text{RRR} = 2$  denotes the residual resistance ratio of our thin-film aluminium, and  $\gamma_0 = 0.1 \text{ eV}/\hbar$  is a phenomenological relaxation rate (dissipation of current). Finally, setting  $\epsilon_0 = 1.03$  as the relative permittivity of aluminium takes into account the core inter-band transitions<sup>54</sup>.

To numerically compute the Casimir pressure in a reasonable amount of time, we take the Matsubara frequencies up to  $\ell = 200,000$ . We determine that this is sufficient by increasing the range of the sum until the final pressure changes by less than  $10^{-5}$  of the value for the previous range. Conversely, to compute the difference between  $\epsilon_{\text{Drude}}$  and  $\epsilon_{\text{BCS}}$  it is sufficient to take<sup>28</sup>  $\ell \lesssim 600$ . Nonetheless, we must also integrate over  $k_{\perp}$ . The integrand of Eq. (5) is sharply peaked<sup>25</sup>, and heuristic bounds of  $\pm 300 \sqrt{\xi_{\ell} \Delta}$  seem to have sufficiently small error.

In Fig. 5, we plot the results of our evaluation of Eq. (5) for our system. While the Casimir pressure scales as  $P \propto d^{-4}$  for ideal conductors<sup>1</sup>, for real conductors the scaling exponent is different. Using the material parameters for aluminium, the pressure is best described by a fit  $P_c = -\frac{1275 \pm 7 \cdot 10^{-24}}{d^{3.193}} \text{ Pa}$ , with the 95% confidence intervals extracted from the fit to the calculation results. We have plotted the dependence  $P \propto d^{-3.193}$  as a black line in Fig. 5.

### Drum design and fabrication

The drum fabrication process starts with a 2-inch quartz wafer. For each patterning step, we spin-coat three resist layers (MMA(8.5)MAA EL7 at 4000 RPM (rotations per minute) for 60 s with a 90 s bake at 150 °C, PMMA 950 A3 at 4000 RPM for 60 s with a 90 s bake at 180 °C, and then Espacer 300Z at 4000 RPM for 60 s with a 60 s bake at 90 °C) and pattern the design by electron beam lithography. Our development recipe is a 30 s bath in a 1:3 mixture of MIBK:IPA, followed by a brief bath and rinse in pure IPA. The first pattern step consists of markers for alignment, so we evaporate

5 nm Ti and 40 nm Au. Then we perform lift-off using a hot acetone bath ( $\approx 55 \text{ }^{\circ}\text{C}$  for 20 minutes followed by 2 minutes in a sonicator bath).

The bottom layer pattern consists of the microwave cavity, bonding pads, waveguides and the bottom plate of the drum resonator. We evaporate a 40 nm Al layer in an electron beam evaporator, and realise the liftoff as described before. Then, we grow a 80 nm layer of amorphous silicon ( $\alpha$ -Si) by PECVD, which forms the sacrificial layer between the drum plates. This layer is patterned with a single layer of PMMA 950 A9, and etched by reactive ion etching using a mixture of  $\text{SF}_6/\text{O}_2$ .

The top layer consists only of the top drum plate. We evaporate a 120 nm Al layer after patterning. Until now, all steps have been performed on a full 2-inch wafer, but after the final Al evaporation we dice the chips to their final  $4 \times 4 \text{ mm}^2$  size. We perform a heat treatment (15 minutes on a hot plate set to between 240 and 280 °C) to redistribute the stress in the top-layer Al and ensure the drums are flat (i.e., not bulging upwards). The final step is the release etch, where we etch the  $\alpha$ -Si sacrificial layer away with a reactive ion etch mixture of  $\text{SF}_6/\text{O}_2$  and get a drum resonator with a suspended top layer.

### Measurement setup

Our setup consists of a sample mounted on the base plate of a Bluefors dilution refrigerator, as schematically shown in Fig. 6. To drive our sample, we source the drive  $a_{\text{mw}}$  at the cavity frequency from a microwave generator, and the drive at the red sideband,  $a_{\text{sb}}$ , from a vector network analyzer. The drive  $a_{\text{sb}}$  is attenuated by a directional coupler that merges it to the main drive  $a_{\text{mw}}$ . Both drives make their way through a suitably attenuated input line to the sample at the base plate of the refrigerator.

The sample is measured in reflection, and the reflected signal is routed through a stack of two circulators and a band-pass filter. A copy of  $a_{\text{mw}}$  split off from the same source is used to interferometrically cancel the drive component reflected from the sample. This is done to avoid saturating the cryogenic amplifier. The cancellation line has a tunable phase delay and attenuation, which we manually set to maximally cancel the output before starting any measurement. On the output line from the sample, after the directional coupler, there is a low-temperature low-noise amplifier, followed by another amplifier at room temperature. Finally, half of the signal is sent back to the network analyzer for measurement, while the other half is routed through a third amplifier to the spectrum analyzer.

Our measurement protocol starts by generating a set of frequencies around the sideband that we will drive. This gives us control over the direction of the frequency sweep. The cavity drive is turned on, then the sideband drive is initialized to the first frequency. We record the signal on the spectrum analyzer while the sideband frequency is swept. We repeat this sequentially for each of the six readout windows, then reverse the frequency sweep direction, and repeat it again for all six readout windows. This stepped protocol means that the sideband drive is briefly turned off to switch to the next frequency,

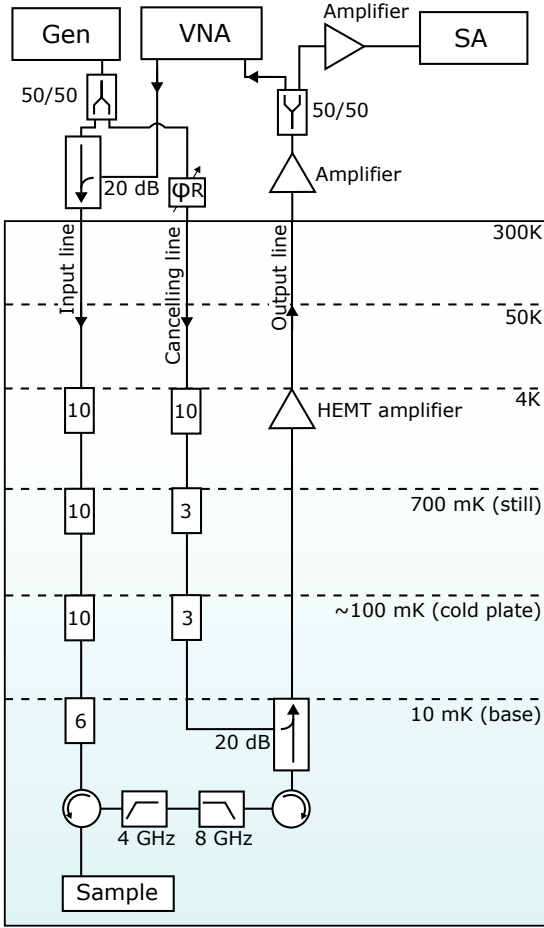


**Fig. 6 | Setup.** Schematic of the setup used in the experiments. The two drives  $a_{mw}$  and  $a_{sb}$  are sourced from a microwave generator (Gen) and a vector network analyzer (VNA) respectively. The output signal is split between the vector network analyzer and a spectrum analyzer (SA). The attenuator values are given in dB.

which can cause the oscillator to decay to the low-amplitude branch. The point on the high-amplitude branch at which this happens is not random, it is reproducible between measurements, as evidenced by the overlap of the curves in Fig. 4b. The stepped drive frequencies do not overlap perfectly with the frequency bins of the spectrum analyzer, and we apply a data filtering scheme detailed in the [Supplementary Information](#).

### Drum frequency and effective mass

The released drums are measured in an atomic force microscope (AFM) to estimate the gap at room temperature. In Fig. 7 the device measured in this work is shown. By comparing the heights at various points on the geometry of the drum, we can estimate the layer thicknesses and gap size. The connector to the right in Fig. 7 is deposited in the first evaporation step, so it provides a height reference for the bottom plate of the drum (purple dotted linecut). The top layer shows

three distinct heights (along the pink dotted linecut): In the drum center the total thickness is contributed by the thickness of the bottom aluminium plate, the thickness of the sacrificial  $\alpha$ -Si layer, and the thickness of the top layer. Closer to the drum edge, the bottom plate stops and only the  $\alpha$ -Si layer and the top layer thicknesses contribute. At the edge of the drum, the top plate contacts the substrate and accounts for the whole thickness. Finally, beyond the drum we measure only the substrate, although the exposed substrate is etched by  $\approx 120$  nm in the drum release step.

We smooth the measurement of the top drum layer and extrapolate it using the known layer thickness to calculate the average gap. The extrapolated gap is shown by dashed black lines in Fig. 7, and it is approximately 100 nm. There is a slight concavity in the middle of the drum of 15 nm. This can be explained by a small tensile stress that remains in the aluminium layer due to fabrication. We model the geometry of the drum in COMSOL and show a cut plane through the center of the drum in Fig. 8a. At room temperature, a 15 MPa tensile stress in the aluminium domain yields a 15 nm concavity that matches the AFM measurement.

When the drum is cooled down, the materials thermally contract, but the contraction of the aluminium is much stronger than that of the quartz. To estimate the relative contractions, we use the temperature dependent material parameters included in COMSOL's basic library, for thin-film aluminium and c-axis quartz (corresponding to our z-cut wafers). We extrapolate the dilation coefficient of quartz below 73 K based on literature values<sup>55</sup>. As a result of the larger relative contraction of the aluminium drum with respect to its substrate, it is subject to an increased tensile stress upon cooling it down to 10 mK. The side walls of the drum unfold and the membrane is brought downwards, which has been previously noted by other groups working with drum resonators<sup>30</sup>. The gap is reduced from 100 nm to 18 nm. Note that this estimate of the drum's separation  $d = 18$  nm (unperturbed by the Casimir force) is found from an entirely independent estimation method from the value of the same parameter  $d = 18.00 \pm 0.25$  nm found by fitting experimental data. While we consider that this simulation method to estimate  $d$  is much less reliable than the fit to experimental data, the fact that these methods independently yield the same value gives confidence in this estimate.

The shape of the fundamental drum mode (Fig. 8b) is negligibly affected by the thermal contraction, but the frequency of the mode is simulated to vary from 5.4 MHz at room temperature to 16.2 MHz at 10 mK. This frequency is the 'unperturbed' frequency in Table 1 that we use as input for the Casimir oscillator simulations. The mechanical mode shape  $\mathbf{u}(\mathbf{r})$  computed using COMSOL is shown in Fig. 8b. Here, the displacement detection and actuation profiles coincide and are commonly denoted  $\mathbf{w}(\mathbf{r})$ . In this case the effective mass is computed as<sup>56</sup>

$$m_{\text{eff}} = m \frac{\int_V \|\mathbf{u}(\mathbf{r})\|^2 d^3\mathbf{r}/V}{\left(\int_V \mathbf{w}(\mathbf{r}) \cdot \mathbf{u}(\mathbf{r}) d^3\mathbf{r}/V\right)^2}, \quad (11)$$

where  $m$  is the physical mass,  $V$  is the volume of the oscillator.

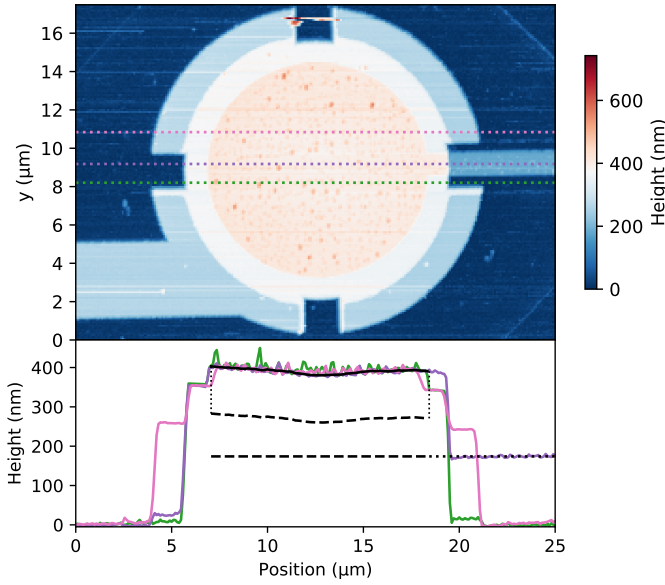
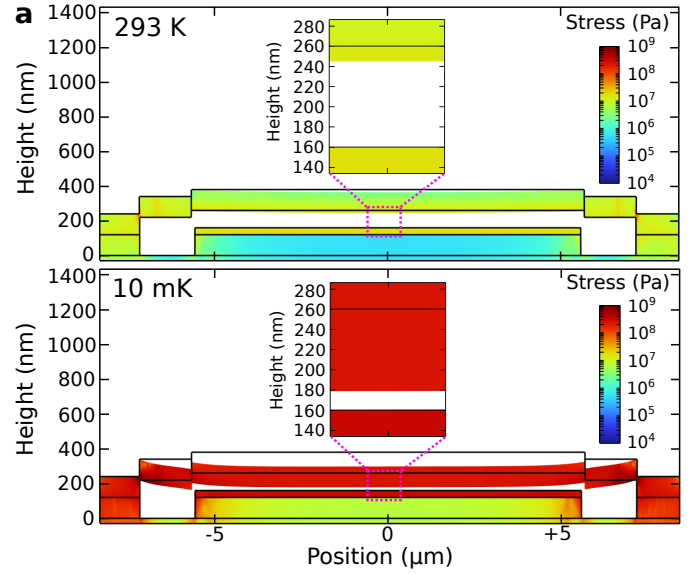


**Fig. 7 | AFM measurement of the superconducting drum.** The room-temperature gap between the superconducting plates can be estimated from an AFM measurement by comparing the heights along different linecuts (colored dotted lines). The purple line provides a height reference for the bottom plate via the exposed connector on the right side; the green line provides a height reference for the (etched) substrate and the pink line provides a height reference to the thickness of the top layer. We extrapolate the gap (dashed black lines) by subtracting the top layer thickness, 120 nm from the smoothed top linecut. There is a slight concavity of the suspended part, approximately 15 nm on an average gap of 100 nm.

The amplitude given to  $\mathbf{u}(\mathbf{r})$  for the computation is irrelevant. In a good approximation, the actuation/detection profile  $\mathbf{w}(\mathbf{r})$  is assumed to be oriented along  $z$ -axis, and to be homogeneous across the bottom plate. The physical mass is calculated to be  $m = 5.35 \cdot 10^{-14}$  kg and the effective mass  $m_{\text{eff}} = 3.96 \cdot 10^{-14}$  kg.

### The Casimir oscillator

In Eq. (1) we have added a strongly nonlinear term to the equation of motion of a harmonic oscillator. It is typical to perform a Taylor expansion of this term for small motions and truncate the resulting series<sup>9,32</sup>, but that approximation fails to describe the higher-amplitude motion seen in our measurements. Instead, we use the MATLAB-based continuation library MatCont<sup>57,58</sup> for our numerical computations, which can handle Eq. (1) without approximations. This toolbox employs different methods for an extensive study of nonlinear dynamics of a system, such as tracking equilibrium points, detecting bifurcations, and continuing branches of periodic solutions. The continuation method involves two steps: iterative prediction of a point on the solution curve and correction of the predicted point through a Newton-like procedure. This procedure is based on linearizing the function at the current guess and finding where the linear approximation intersects



**b** Drum mode 293K: 5.4 MHz  
10 mK: 16.2 MHz

**Fig. 8 | Simulated drum mechanics.** **a:** A plane cut through the center of the simulated drum geometry shows a 15 nm concavity if a 15 MPa tensile pre-stress is included in the aluminium domain. By cooling down to 10 mK, the aluminium contracts more than the quartz substrate, which greatly increases the tensile stress in the drum. Under this tensile stress, the torque applied on the edges of the drum brings it downwards which reduces the vacuum gap from 100 nm to very low values consistent with the experimentally determined 18 nm according to simulations. **b:** Simulated mode shape and frequencies of the drum. The fundamental drum mode greatly increases in frequency due to the added tensile stress.

with the  $x$ -axis, which becomes the next approximation.

For MatCont, the system of equations must be of the first-order and autonomous (no explicit time dependence). The drive term of Eq. (1),  $F_0 = F_d \sin(\omega_d t)$ , is the only term explicitly dependent on time. We can make it autonomous by using the Hopf normal form which allows us to express the dynamics in terms of two real variables in amplitude-phase form. Hopf normal form in Cartesian coordinates reads

$$\begin{aligned} \dot{u} &= (\mu - x^2 - y^2)x - \omega_d y \\ \dot{v} &= (\mu - x^2 - y^2)y + \omega_d x \end{aligned} \quad (12)$$

Assuming  $\mu = 1$ , we choose  $u$  to substitute the drive term.

We non-dimensionalize and scale Eq. (1), and split it into two first-order equations. We define,

$$x' = \frac{x}{x_0}, \quad t' = \frac{t}{t_0}, \quad \text{and} \quad y = \dot{x} \quad (13)$$

where  $x_0 = 10^{-9}$  m and  $t_0 = 2\pi/\omega_r$ .

Substituting all, our system of equations become:

$$\begin{aligned}
 \dot{x} &= y, \\
 \dot{y} &= -Ay - Bx - C(x+d)^n + Du, \\
 \dot{u} &= u(1 - u^2 - v^2) - \Omega u, \\
 \dot{v} &= v(1 - u^2 - v^2) + \Omega v,
 \end{aligned} \tag{14}$$

with  $A = t_0 \gamma_r$ ,  $B = t_0^2 \omega_r^2$ , and

$$C = \frac{t_0^2 P_c \pi r^2 d^n}{m_{\text{eff}}(x_0)^{n+1}}, \quad \text{and} \quad D = \frac{t_0^2 F_d}{m_{\text{eff}} x_0}. \tag{15}$$

We apply a periodic forcing to the system by arbitrarily choosing  $u = 1$ ,  $v = 0$ . First, we perform an extended simulation until the system converges to a limit cycle. The last orbit provides the initial conditions for the continuation simulation. By varying certain parameters such as the drive force amplitude  $F_d$ , damping coefficient  $\gamma_r$ , separation distance  $d$  and the Casimir exponent  $n$ , we study how the system's response is affected.

We have become aware of a recent work studying the Casimir force across a superconducting transition<sup>59</sup>.

#### *Data and code availability*

All data, simulations, measurement and analysis scripts in this work are available at <https://doi.org/10.5281/zenodo.14700381>.

#### *Acknowledgments*

We would like to acknowledge Gongchang Lin for help with the AFM and Eddy Collin for help with the geometric non-linearity. We acknowledge the facilities and technical support of Otaniemi research infrastructure for Micro and Nanotechnologies (OtaNano), and the Aalto Scientific Computing team for their support. L.M.d.L. acknowledges funding from the Strategic Research Council at the Academy of Finland (Grant No. 338565).

#### *Author contributions*

M.d.J., E.K., L.B., and L.M.d.L. designed, developed, and performed the experiments. L.B. developed and fabricated the device, L.M.d.L, M.d.J. and E.K. developed the theoretical and numerical analysis. L.M.d.L. conceptualized the project and L.M.d.L. and M.A.S. oversaw it. All authors contributed to writing and editing the manuscript.

#### *Competing interest declaration*

The authors declare no competing interests.

## SUPPLEMENTARY INFORMATION

This part of the document contains the supplementary information.

### A. Optomechanical description

#### 1. Equations of motion

The optomechanical equations of motion for a single mechanical mode coupled to a single cavity mode are<sup>48</sup>:

$$\begin{aligned}\hat{x}(t) &= \omega_m \hat{p}, \\ \dot{\hat{p}}(t) &= -\omega_m \hat{x} - \gamma_m \hat{p} - g_0 \hat{a}^\dagger \hat{a} + \sqrt{\gamma_m} \hat{\xi}(t), \\ \dot{\hat{a}}(t) &= -(i\Delta + \kappa/2)\hat{a} + ig_0 \hat{x} \hat{a} - \sqrt{\kappa_e} \hat{s}_{\text{in}}(t) - \sqrt{\kappa} \hat{a}_{\text{noise}}(t).\end{aligned}\quad (\text{S1})$$

We use operators  $\hat{x}$  and  $\hat{p}$  to refer to the position and momentum of the mechanical resonator respectively, and  $\hat{a}$  denotes the cavity mode field amplitude. The mechanical parameters  $\omega_m$ ,  $\gamma_m$ , the cavity parameters  $\kappa$ ,  $\Delta$ , and the coupling strength  $g_0$  are the same as in the main text and their values are listed in Table I. Note that we use the mechanical parameters  $\omega_m$  and  $\gamma_m$  which are the 'dressed' parameters from the Casimir force rather than the 'unperturbed' parameters  $\omega_r$  and  $\gamma_r$ . We operate in a frame rotating at the frequency of the microwave drive, and have noise terms  $\hat{\xi}(t)$  and  $\hat{a}_{\text{noise}}(t)$ . Our system is strongly driven, so we can safely neglect the noise terms in the majority of numerical simulations. The input field is a combination of the (strong) drive at the microwave cavity frequency, and a weaker sideband drive. It can be expressed as

$$\hat{s}_{\text{in}}(t) = \sqrt{P_{\text{mw}}/\hbar\omega_c} + \sqrt{P_{\text{sb}}/\hbar\omega_c} e^{-i\omega_m t}. \quad (\text{S2})$$

This is enough to solve the system of equations of motion for some initial conditions  $\hat{x}(0)$ ,  $\hat{p}(0)$ , and  $\hat{a}(0)$ . However, to translate the motion of the resonator into the signal we detect, we have to model our detection scheme as well. We use input-output theory to compute the output fields

$$\hat{a}_{\text{out}} = \sqrt{\kappa_e} \hat{a} - \hat{s}_{\text{in}}. \quad (\text{S3})$$

We finally compute the spectrum of the output field that we measure by using the Fourier transform  $\mathcal{F}$ ,

$$S_{\text{out}}(\omega) = \left| \mathcal{F} \left\{ (\hat{a}_{\text{out}} + \hat{a}_{\text{out}}^\dagger)/2 \right\} \right|^2. \quad (\text{S4})$$

This spectrum  $S_{\text{out}}(\omega)$  is what we record on the spectrum analyzer.

We can independently calibrate the parameters  $\omega_m$ ,  $\gamma_m$ ,  $\kappa$ ,  $\Delta$ , and  $g_0$  as reported in Sec. C. We also accurately know the powers of the cavity and sideband drive tones we send in, but between the output of the generators and the cavity are attenuators and cable losses (see [Methods](#)). To calibrate the amplitudes of our drives at the cavity entrance, we first make a crude estimation based on the relative sideband powers (next section), and then refine that using the full optomechanical equations of motion (section after that).

### 2. Relative sideband powers

We have recorded the powers of six sidebands ( $\pm\omega_m$ ,  $\pm 2\omega_m$ , and  $\pm 3\omega_m$ ) for the measurements reported in the main text. We can compare the relative powers of each of the sidebands, and compare the powers with the sideband drive, to show how our detected signal is proportional to the mechanical displacement. We use the perturbative treatment of the classical coupled mode equations<sup>48,49</sup>. Our starting point is a simplified version of Eqs. (60) and (61) of Ref.<sup>48</sup>, where the steady state cavity field amplitude  $a_0$  is defined by the input power of the microwave drive at the cavity frequency,  $a_{\text{mw}}$ , and cavity parameters  $\kappa_e$ ,  $\Delta$  and  $\kappa$ .

$$\begin{aligned}a_0 &= a_{\text{mw}} \frac{\sqrt{\kappa_e}}{-i\Delta + \kappa/2} \\ a_{+1} &= \frac{g_0 x_{\text{amp}}}{2x_{\text{zpf}}} \frac{a_0}{-i(\Delta + \omega_m) + \kappa/2} \\ a_{-1} &= \frac{g_0 x_{\text{amp}}}{2x_{\text{zpf}}} \frac{a_0}{-i(\Delta - \omega_m) + \kappa/2}.\end{aligned}\quad (\text{S5})$$

Here, the amplitude of the anti-Stokes- and Stokes-scattered sidebands are denoted with  $a_{+1}$  and  $a_{-1}$  respectively. These exist in the spectrum at  $\pm\omega_m$  away from the frequency of  $a_0$ , and they are related to the mechanical amplitude  $x_{\text{amp}}$ .

Our six-sideband treatment is based on repeating the treatment of Eq. (S5), but considering  $a_{\pm 1,2,3}$  as the source term instead of  $a_0$ . That is, from  $a_{+1}$  we recognize two scattering processes, which end up at  $a_0$  and  $a_{+2}$  respectively.

$$\begin{aligned}a_0 &= + \frac{g_0 x_{\text{amp}}}{2x_{\text{zpf}}} \frac{a_{+1}}{-i\Delta + \kappa/2} \\ a_{+2} &= \frac{g_0 x_{\text{amp}}}{2x_{\text{zpf}}} \frac{a_{+1}}{-i(\Delta + 2\omega_m) + \kappa/2}\end{aligned}\quad (\text{S6})$$

By repeating this treatment for all orders of sidebands that we measure, we gain a set of linear coupled equations. This resulting system can be written in matrix form as

$$\begin{bmatrix} 1 & d_{+3} & 0 & 0 & 0 & 0 & 0 \\ d_{+2} & 1 & d_{+2} & 0 & 0 & 0 & 0 \\ 0 & d_{+1} & 1 & d_{+1} & 0 & 0 & 0 \\ 0 & 0 & d_0 & 1 & d_0 & 0 & 0 \\ 0 & 0 & 0 & d_{-1} & 1 & d_{-1} & 0 \\ 0 & 0 & 0 & 0 & d_{-2} & 1 & d_{-2} \\ 0 & 0 & 0 & 0 & 0 & d_{-3} & 1 \end{bmatrix} \begin{bmatrix} a_{+3} \\ a_{+2} \\ a_{+1} \\ a_0 \\ a_{-1} \\ a_{-2} \\ a_{-3} \end{bmatrix} = \begin{bmatrix} 0 \\ 0 \\ 0 \\ \frac{a_{\text{mw}} \sqrt{\kappa_e}}{-i\Delta + \kappa/2} \\ 0 \\ 0 \\ 0 \end{bmatrix} \quad (\text{S7})$$

with

$$d_{\pm n} = \frac{g_0 x_{\text{amp}}}{2x_{\text{zpf}}} \frac{1}{-i(\Delta \pm n\omega_m) + \kappa/2}. \quad (\text{S8})$$

We have made the simplifying assumption that repeated interactions ending up at lower-order sideband are negligible in power compared to the (original) lower-order sideband power. This is a valid assumption when  $g_0 \ll \kappa/2$ , since each individual photon is much more likely to exit the cavity than to scatter from the mechanical resonator.

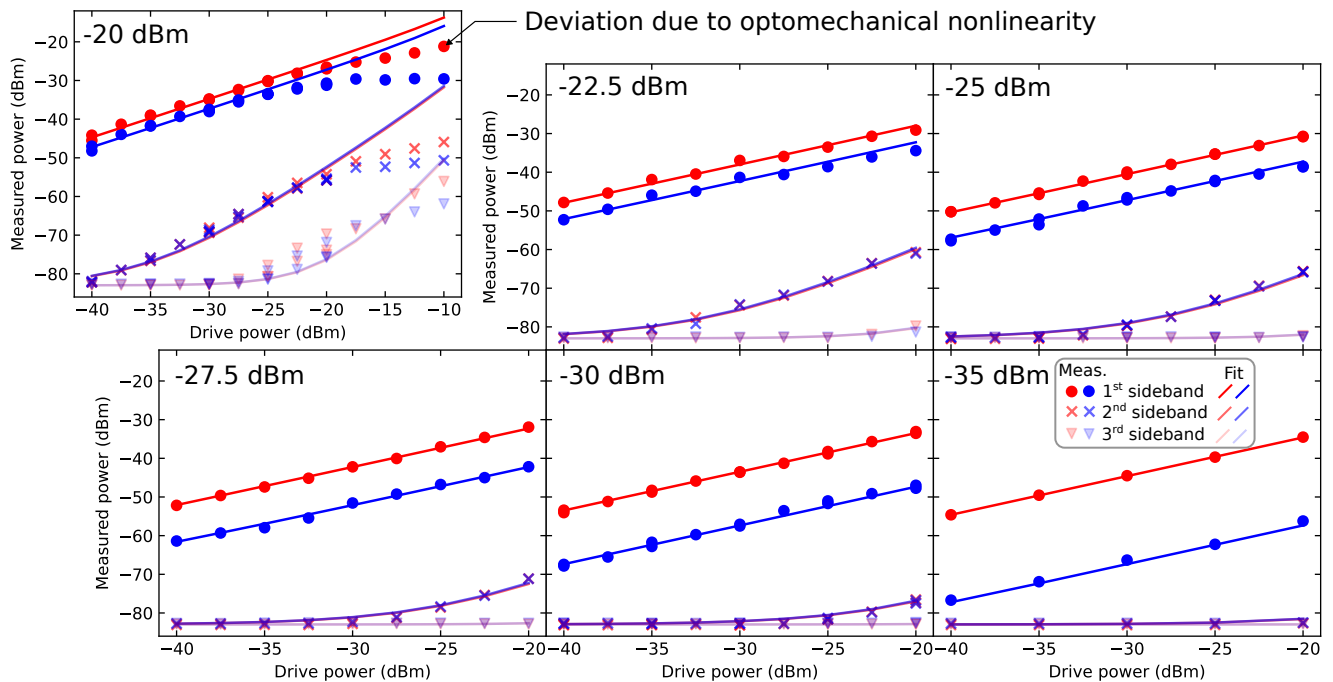


**Fig. S1 | Relative sideband powers.** Comparison of the maximum powers in all 6 sidebands for different powers of cavity drive  $a_{mw}$  (panel labels) and sideband drive  $a_{sb}$  (x-axis). The colors indicate whether the sideband is on the red side of the cavity ( $a_{-1,-2,-3}$ ) or on the blue side ( $a_{+1,+2,+3}$ ). The markers are measurements, solid lines are fits to the model of Eq. (S10). Only at the highest powers does our model deviate from the data, which is due to the optomechanical nonlinearity. The asymmetry of the first-order sidebands provides a power reference between the applied drives. The higher order sidebands are symmetric, so they overlap and appear purple in the plot. This symmetry motivates neglecting the scattering processes of  $a_{sb}$  which we have done in constructing Eq. (3).

It is fairly straightforward to numerically solve Eq. (S7) using e.g., Python. This model is valid when the optomechanical interaction is dominated by a single drive tone, which in our case is  $a_{mw}$ . However, we have a weaker second drive,  $a_{sb}$ , at  $-\omega_m$ . Since it is much weaker than  $a_{mw}$ , we neglect the effect of any scattering interactions from  $a_{sb}$  on the sideband amplitudes. The result of this is that there is an asymmetry only between the first-order red ( $a_{-1}$ ) and blue ( $a_{+1}$ ) sidebands. If we had included the scattering interactions of the weaker drive, the red and blue sidebands of all orders would have the same asymmetry. However, from the measurements we will see that this is not the case (only the first order sidebands are asymmetric), and therefore we neglect the scattering interactions of  $a_{sb}$  in our sideband amplitude calculation. Thus the resulting amplitude(s) due to this drive are

$$\vec{a}_{sb} = \begin{bmatrix} 0 \\ 0 \\ 0 \\ 0 \\ \frac{a_{sb} \sqrt{\kappa_c}}{(-i(\Delta - \omega_m) + \kappa/2)} \\ 0 \\ 0 \end{bmatrix}. \quad (\text{S9})$$

To fit this model to our data, we solve Eq. (S7) for  $\vec{a}$  and compute the output field using the input-output formalism. Here we also add the solution for the weaker drive field  $a_{sb}$ .

The output field is described by

$$a_{out} = \sqrt{\kappa_c} (\vec{a} + \vec{a}_{sb}) - \begin{bmatrix} 0 \\ 0 \\ 0 \\ \frac{a_{mw}}{-i\Delta + \kappa/2} \\ \frac{a_{sb}}{-i(\Delta - \omega_m) + \kappa/2} \\ 0 \\ 0 \end{bmatrix} \quad (\text{S10})$$

In Fig. S1 we have plotted the maximum observed powers of each of our measured sidebands (markers) for different drive powers, and compared those to our fitted model (solid lines). There is an excellent agreement at all but the highest powers. For the highest powers, the optomechanical nonlinearity reduces the drive efficiency, which reduces the maximum powers seen in the sidebands.

The measurements record the sideband powers, and from our model we extract  $|a_{out}|^2$ , but we need two conversion factors to link the theory to our experiments (one for each axis of Fig. S1). There is also attenuation from the room-temperature source to the cavity at 10 mK (see Methods), which gives us an additional conversion factor. The simplifications of the model of Eq. (S7) are not ideal to use it as an accurate calibration tool between mechanical amplitude and measured power, but it serves as a quick estimation of these conversion factors. We use these as an initial guess for the simulation-based calibration method using the optomechanical equations of motion de-

scribed in the next section.

### 3. Absolute amplitude calibration

The optomechanical equations of motion, Eq. (S1), provide us with a method to calibrate the mechanical amplitude, since they do not depend on the distance  $d$  or the Casimir parameters, pressure  $P_c$  and scaling  $n$ . At small amplitudes, our resonator behaves like a harmonic oscillator since the Casimir effect does not perturb small dynamical motion. To calibrate the mechanical amplitude, we need to know the optomechanical parameters of the system, which we characterize in Sec. C, and the total attenuation between microwave source/vector network analyzer and the cavity entrance. We know the attenuator values on our input line (see Fig. 6), but we do not accurately know the cable loss.

To model our system, we extract the peak power observed on the first red and first blue sideband ( $\omega_c \pm \omega_m$ ) and the power in the drive pedestal on the red sideband. Then we let Eq. (S1) evolve numerically until it has settled into a steady state, and simulate the steady state for 10 ms. We compute the Fourier transform of the output field, as in Eq. (S4), which gives us the observed power, while we obtain the mechanical oscillation amplitude from the size of the orbit of  $\hat{x}$ ,  $\hat{p}$  of Eq. (S1). We repeat this for all combinations of the cavity drive and sideband drive power ( $P_{mw}$  and  $P_{sb}$  respectively). The final observed spectrum of Eq. (S4) is multiplied with the scale factor (W/phonon)  $S_c$  found in Sec. C, compensated for the measurement bandwidth in the experiment and the finite simulation time.

We find good agreement between the experimentally observed powers and the simulations for a cable loss of 47.4 dB (of which 36 dB comes from the installed attenuators), and a 22.2 dB reduction of  $P_{sb}$  with respect to  $P_{mw}$ , which we attribute to the directional coupler. At these values, the simulated powers of the resonance peaks match the measured powers, as shown in Fig. S2 for the red (A) and blue (B) sidebands. At low power, the agreement between the simulations and measurements is good, but at high powers the Casimir effect starts to play a large role in the experiments, and the simulations overestimate the power. The simulated curves become less steep, but this is due to the optomechanical drive efficiency discussed in the main text and in the next section. The grey shaded area indicates the detection noise floor.

We repeat the numerical simulation for a 3 kHz detuned sideband drive, to simulate the sideband drive pedestal on the red sideband. All simulations fall on a perfect straight line that matches the experimental observations, as shown in Fig. S3. The combination of the off-resonant drive and the relative on-resonant powers in the red and blue sidebands provide an absolute reference of power that is independent of our detection efficiency or any amplifiers between resonator and detector.

The simulated amplitudes achieved by the mechanical resonator for all combinations of cavity and sideband drive powers are shown in Fig. S4. At small amplitudes, the maximum amplitude scales linearly with both cavity and sideband drive powers, but at some point this relation breaks down due to

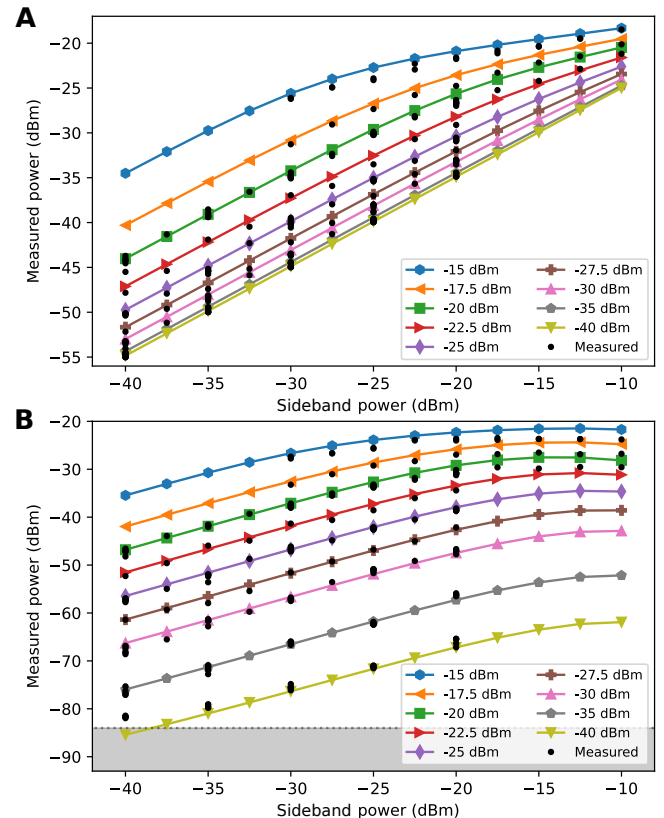


**Fig. S2 | Sideband calibration.** A Simulated powers (colored lines with various markers) and observed peak powers (black dots) for the red sideband. The legend indicates  $P_{mw}$ , the x-axis is  $P_{sb}$ . The agreement between the simulations and the measurements at low power serves as a calibration for the numerical simulations. B Idem, but for the blue sideband. The grey shaded area shows the noise floor for the measurements.

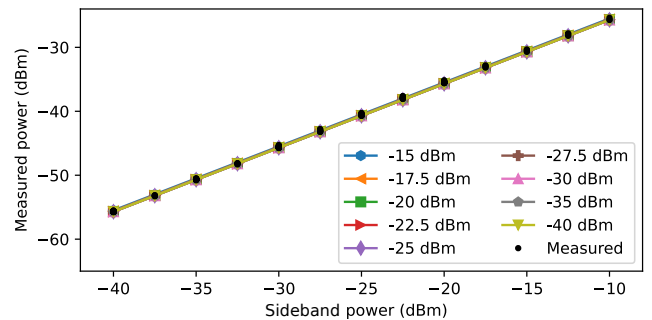


**Fig. S3 | Input power calibration.** The 3 kHz off-resonant drive simulations show a perfect overlap between all simulated (colored markers) and measured powers (black dots).

the drive efficiency. This drive efficiency deforms the Casimir curves we simulate, but it only flattens the top as shown in Fig. 3, and it does not affect the parts of the curve where the mechanical amplitude is small. To accurately choose a maximum amplitude of the Casimir curve we simulate in MatCont, we thus extrapolate the amplitude that the curve should have

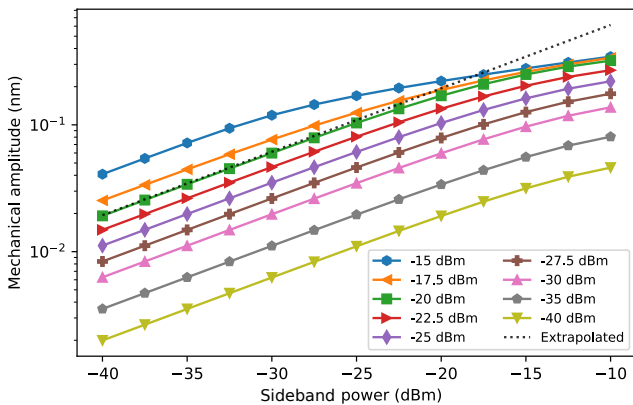


**Fig. S4 | Calibrated mechanical amplitude.** Calibrated amplitude achieved by the mechanical resonator for different combinations of cavity and sideband drive powers.

gotten without the drive efficiency. For this, we follow the linear parts of the curve at low power and extrapolate as indicated by the dotted line in Fig. S4 for the  $-20$  dBm data set.

#### 4. Calculation of the drive efficiency

The tenet of (dispersive) cavity optomechanics is that the cavity frequency  $\omega_c$  shifts as a result of the mechanical position  $x$ <sup>48</sup>. In this work, the amplitude of  $x$  is significant, and the cavity frequency shift  $\frac{\partial\omega_c}{\partial x}$  causes a mismatch between the cavity frequency and the drive frequencies,  $\omega_{mw} \simeq \omega_c$  and  $\omega_{sb} \simeq \omega_c - \omega_m$ . The cavity frequency  $\omega_c(t)$  is thus a function of time, it oscillates at  $\omega_m$  depending on the exact trajectory of the drum.

To put it simply, for larger oscillations of  $x$ , the frequency mismatch between cavity and drive is greater and the power in the cavity decreases. The oscillation is fast with respect to the cavity linewidth, as we are in the resolved sideband limit  $\kappa \ll \omega_m$ , which means that the cavity amplitude changes slowly with respect to the oscillation of  $\omega_m$ . Furthermore, we also have two drives separated in frequency. So while the power resulting from the drive at  $\omega_c$  is maximal for small motions of  $x$ , the power resulting from the drive at  $\omega_c - \omega_m$  peaks for some specific oscillation amplitude of  $x$ .

We calculate the drive efficiency by solving Eq. (S1) for  $\gamma_m = 0$  such that the mechanical amplitude is fixed at the initial value we set for  $x(t = 0)$ . We let the system simulate only for a brief time, such that the cavity amplitude  $a$  has had time to stabilize but not enough time that the driving force affects the amplitude  $x$ . A good time span for this is  $1600(\omega_m)^{-1} \simeq 80(\kappa)^{-1}$ . From the last 20 mechanical periods, we extract the power in the cavity. This brief simulation is repeated for 101 values of  $x$  logarithmically spaced between 1 pm and 1 nm for all different cavity drive powers used in the experiments.

In the regime that is relevant for our experiment, the drive efficiency is 1 for small mechanical amplitudes ( $< 100$  pm), and decreases quickly towards zero beyond that. However, at

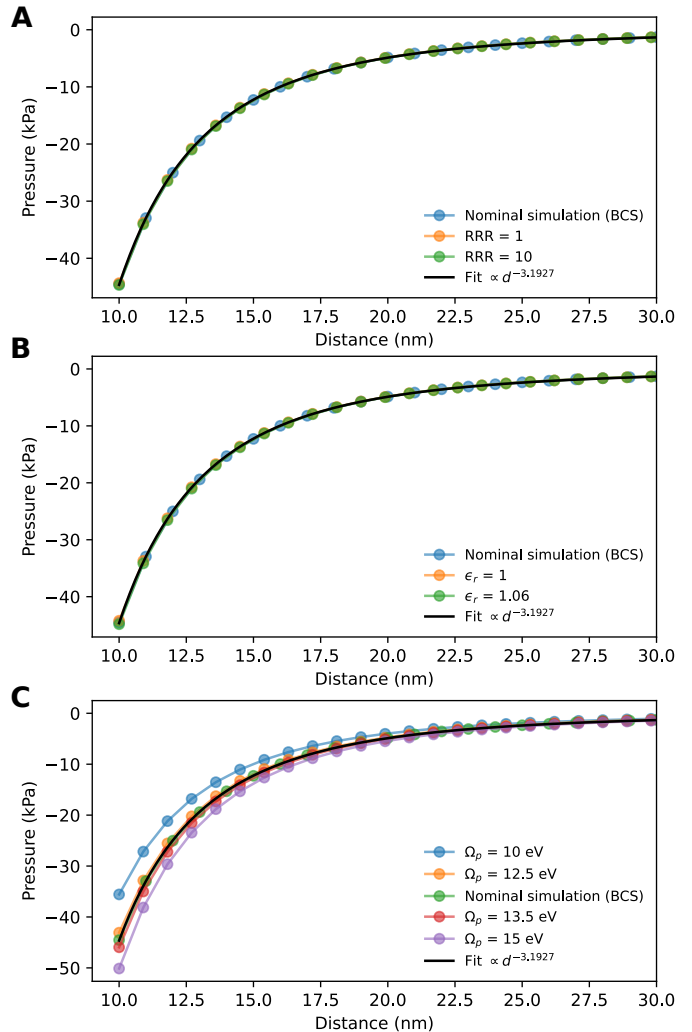


**Fig. S5 | Effect of material parameters.** **A:** The residual resistance ratio (RRR) rescales the dissipation rate  $\gamma_p = \gamma_0/\text{RRR}$ , but varying it from the nominal value  $\text{RRR} = 2$  does not significantly affect the Casimir pressure. **B:** Varying the relative permittivity of aluminium from the nominal value  $\epsilon_r = 1.03$  does not significantly affect the Casimir pressure. **C:** Varying the plasma frequency from the nominal value  $\Omega_p = 13$  eV affect the Casimir pressure amplitude  $P$  more strongly than the Casimir scaling  $n$ .

even larger mechanical amplitudes, beyond what we achieve in this work, the drive efficiency recovers to a non-negligible number in a series of bands that represent stable orbits as described in Ref.<sup>60</sup>.

## B. Simulating the Casimir nonlinearity

### 1. Role of Casimir parameters

We perform the fit of distance  $d$  without considering variations in the calculated Casimir pressure, i.e., we consider the Casimir pressure amplitude  $P$  and scaling  $n$  to be fixed. To motivate this choice, we show that the Casimir pressure does

not vary much with the material parameters  $\gamma_0$  (or RRR),  $\epsilon_0$ , and  $\Omega_p$ . We repeat the Casimir pressure calculations for different material parameters, as shown in Fig. S5, and we fit curves of the form  $P_c = P/d^n$  to distinguish changes in the amplitude of the Casimir pressure ( $P$ ) from changes in the Casimir scaling ( $n$ ).

The residual resistivity ratio, RRR, can vary depending on the material source and deposition method. We have previously measured that our aluminium has RRR = 2 using a four-point probe method. Variations in the RRR affect the phenomenological dissipation rate,  $\gamma_p = \gamma_0/\text{RRR}$ , so Fig. S5A shows the effect of varying either RRR or  $\gamma_0$ . From the overlap between the curves, we conclude that RRR or  $\gamma_0$  affect neither the Casimir pressure amplitude  $P$  nor the Casimir scaling  $n$ .

The relative permittivity of aluminium,  $\epsilon_r = 1.03$  was experimentally determined and follows from the core-interband transitions of the aluminium atoms<sup>54</sup>. We show in Fig. S5 that variations in this parameter do not lead to significant changes in the Casimir pressure.

The plasma frequency of aluminium provides the upper frequency cutoff above which the material becomes transparent to the electromagnetic fluctuations that yield the Casimir effect. We take  $\Omega_p = 13$  eV from Ref.<sup>54</sup>. In Fig. S5 we show that varying  $\Omega_p$  changes the Casimir pressure, but its effect on the Casimir scaling is marginal. A 25% variation in  $\Omega_p$  corresponds to a 25% variation in  $P$ , but less than 1% variation in  $n$ .

To further motivate our choice to consider the calculated Casimir parameters as fixed values, we fit our experimental data to the Casimir force calculated with  $\Omega_p = 10$  and 15 eV. The results are shown in Fig. S6, where we have taken the optomechanical calibration of mechanical amplitude to be fixed. Taking  $\Omega_p = 10$  eV (Fig. S6A), the Casimir force is weaker, which means that to experience the same nonlinearity at fixed mechanical amplitude, the plate separation  $d$  must be reduced. Vice versa, taking  $\Omega_p = 15$  eV (Fig. S6B) leads to a better fit at larger  $d$ . The variations in  $\Omega_p$  are significant (25% of the total value), and well beyond the uncertainty of which the plasma frequency is established in aluminium, yet the effect on the fitted parameter  $d$  is limited ( $\sim 1$  nm). Thus, we conclude that our choice to take the Casimir pressure amplitude and scaling to be fixed values leads to a smaller error than the optomechanical amplitude calibration does.

## 2. Static shift of frequency and position

As we illustrated in Fig. 1A, we start with a harmonic oscillator centered at distance  $d$  from the other plate with unperturbed resonance frequency  $\omega_r$ . The Casimir force pulls the top plate closer to the bottom plate, such that it oscillates around some value  $d' < d$ , and softens the spring so the mechanical frequency is decreased,  $\omega_m < \omega_r$ . We do not know  $d$  or  $\omega_r$  a priori, but we can measure  $\omega_m$  with great accuracy, leaving us to consider  $d$  (or somewhat equivalently the Casimir pressure  $P_c$ ) as a parameter to be fitted. That means that for every value  $d$ , we have to find the value of the

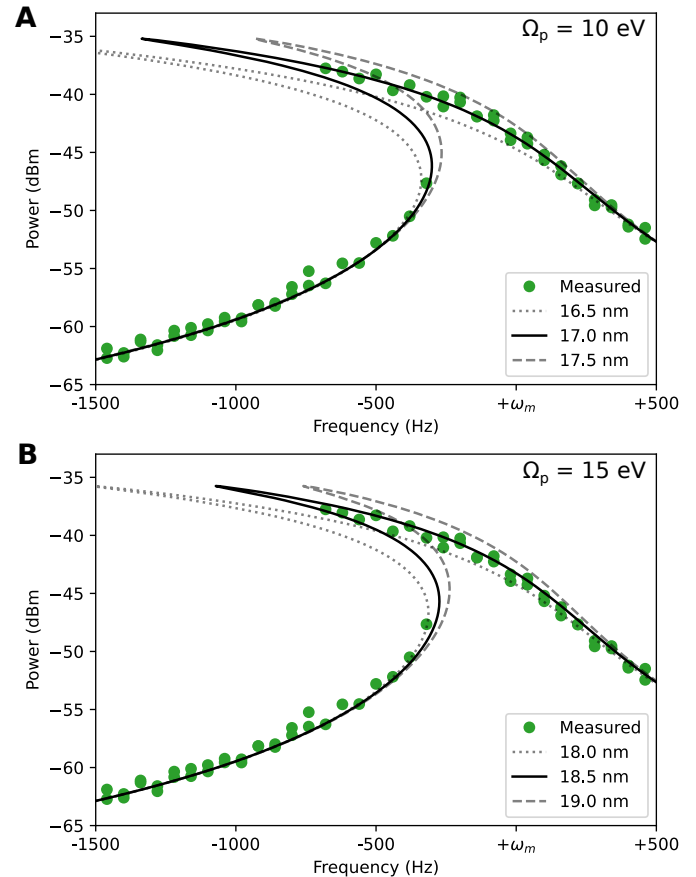


**Fig. S6 | Fits for Casimir force variations.** **A:** The Casimir force for a material with plasma frequency  $\omega_p = 10$  eV is weaker than the nominal Casimir force used in this work. The Casimir nonlinearity fits to a plate separation of  $d = 17.00 \pm 0.25$  nm. **B:** The Casimir force for a material with plasma frequency  $\omega_p = 15$  eV fits to a plate separation of  $d = 18.50 \pm 0.25$  nm.

unperturbed frequency  $\omega_r$  such that the perturbed frequency  $\omega_m = 2\pi \times 10.001$  MHz. Rather than finding a clever algorithm to compute the correct values of  $\omega_r$ , we numerically evaluate the problem for a selection of  $d$ -values and interpolate. In Fig. S7 we show the frequencies  $\omega_r$  that result in the correct value of  $\omega_m$  for different values of  $d$ .

The numerical simulations of the Casimir oscillator in MatCont start with the drive frequency far detuned. To start the continuation, we need this step to converge to a solution. However, the total potential sketched in Fig. 1A has a local minimum (where our resonator is) and a global minimum beyond the pull-in point. We need to feed MatCont the correct initial values such that it converges to the local minimum instead of showing us the pull-in collapse. To find these, we compute the position of the local minimum of the total potential for various values of  $d$ , while using the values of  $\omega_r$  from Fig. S7. The unperturbed frequency  $\omega_r$  is related to the mechanical stiffness needed to compute the potential, not  $\omega_m$ . We plot the stable position of the local minimum for different values of  $d$  in Fig. S8. As with the unperturbed frequencies, we interpolate linearly between the calculated values for the

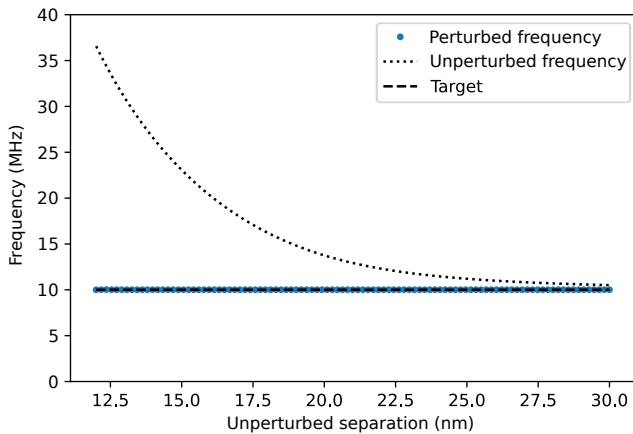


**Fig. S7 | Casimir frequency shift.** Plot of the unperturbed frequencies  $\omega_r$  for various values of spacing  $d$  that result in the correct value for  $\omega_m$  when the Casimir force is included.

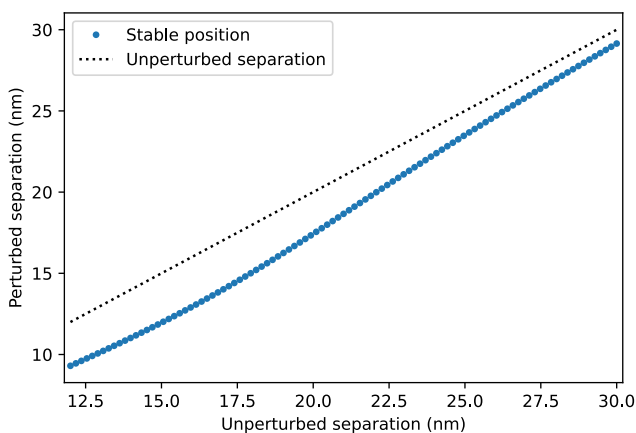


**Fig. S8 | Shift of the local potential minimum due to the Casimir force.** Distance between the local minimum (stable position) and the bottom plate for various values of the unperturbed separation  $d$ . The dotted line indicates where the initial separation would be the stable position. For  $d = 18.0$  nm, the difference between the unperturbed separation and the local minimum is 2.9 nm.

numerical simulations and fits of the main text.

### 3. Role of mechanical parameters

We study the effect of variations of the parameters of the Casimir effect through numerical simulations. We vary the drive force amplitude  $F_d$ , damping coefficient  $\gamma_r$ , separation distance  $d$ , and the Casimir exponent  $n$ . The results are shown in Figure S9.

We show how the system response transforms from linear behavior at small amplitude to nonlinear behavior at large amplitude in Fig. S9A. When the drive force amplitude is small,  $F_d = 10$  fN, the frequency response of the system is Lorentzian, as expected. For larger amplitudes, the resonance peak broadens and becomes asymmetrical, indicative of non-

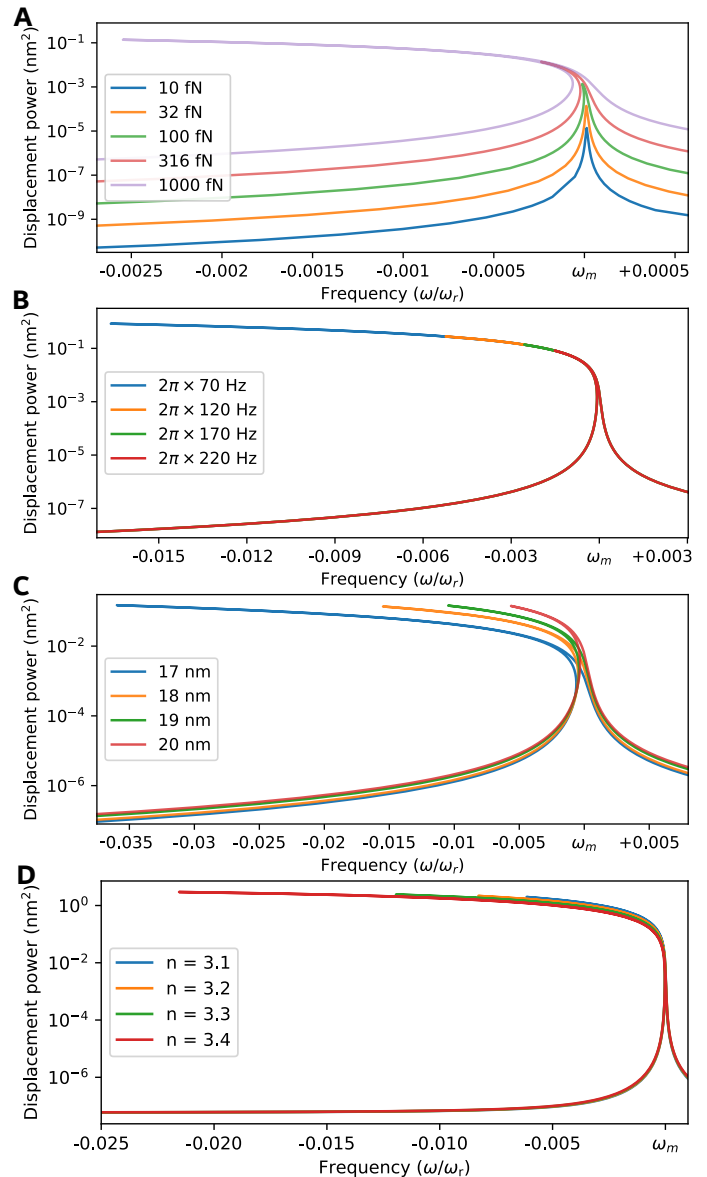


**Fig. S9 | Effect of the Casimir force parameters.** **A:** Effect of different drive force amplitudes  $F_d$ . **B:** Effect of varying the damping coefficient  $\gamma_r$ . **C:** Effect of varying the distance between the plates at mechanical zero.  $d$ . The frequencies of the curves have been shifted to align on  $\omega_m$ . **D:** Effect of varying the Casimir scaling  $n$ , where the amplitude of the Casimir pressure has been fixed at the equilibrium position  $d'$ .

linear resonance where the response of the system is no longer linearly proportional to the drive force. The resonance frequency decreases with increasing amplitude, which indicates that the Casimir force is a strong softening nonlinearity.

In Fig. S9B, we study the effect of the mechanical damping rate  $\gamma_r$ . Lower damping allows for greater energy accumulation within the system at equal drive amplitudes, leading to larger oscillations and a more pronounced nonlinearity. However, all the backbones of the curves for different damping rates align, meaning the damping coefficient does not have a

significant effect on the nonlinearity we observe.

The most important parameter for Casimir experiments is the separation distance  $d$ , which is the distance between the plates in the absence of the Casimir force. Since the Casimir effect strongly scales with the distance  $d$ , the Casimir force between drums spaced  $d = 17$  nm apart (blue curve in Fig. S9C) causes a much stronger nonlinear behavior than for drums spaced  $d = 18$  nm apart. The region where there are multiple solutions is much more extended, even if the amplitude of the mechanical oscillations remains the same. All curves were generated using the same drive force, which indicates that the separation distance  $d$  does not affect the mechanical amplitude significantly.

Finally, we show the effect of the Casimir force exponent  $n$  in Fig. S9D. The Casimir pressure was adjusted for each  $n$  such that the value at the equilibrium position ( $d'$ ) was kept constant. While the trend from the change in  $n$  somewhat resembles the trend from the change in  $d$ , it is noticeable that the peaks curve more sharply with increasing  $n$ , while they start curving at lower amplitude for lower  $d$ .

### C. Characterization of optomechanical system

#### 1. Calibration of the microwave cavity

Our microwave cavity design was optimized to allow coupling to two separate drum resonators with two cavity modes, as shown in Fig. S10A, and described in more detail in the Supplementary of Ref.<sup>39</sup>. In our device, one of the drum resonators inadvertently collapsed and shorted one half of the cavity, though this cannot be seen in the microscope image. Instead, we deduce this by the number of microwave modes we see (one), its frequency ( $\omega_c = 2\pi \times 5.46180$  GHz), and the number of mechanical signals we can observe in a wide-band frequency sweep at high red-sideband drive power (one).

We simulate our cavity using Sonnet, where we have replaced the collapsed drum by a short (Fig. S10B). At first, we replace the suspended drum by a numerical capacitance. An initial guess for the capacitance of this drum based on the diameter  $2r = 11.3$   $\mu\text{m}$  and a gap of 15.1 nm is 0.059 pF. To provide an initial estimate of the optomechanical coupling, we vary the spacing of the vacuum layer in our Sonnet model, and re-compute the cavity resonance frequency. We find  $\frac{\Delta\omega_c}{\Delta x} \simeq 2\pi \times 104$  MHz nm<sup>-1</sup>. We use the zero point motion  $x_{zpf} = \sqrt{\frac{\hbar}{2m_{\text{eff}}\omega_m}} = 4.6$  fm and estimate the coupling rate  $g_0 \simeq x_{zpf} \frac{\Delta\omega_c}{\Delta x} \simeq 2\pi \times 480$  Hz. This is larger than the coupling rate that we find when we calibrate our system by about a factor 3, which we attribute to details not captured by our simulation: microscopic defects or fabrication imperfections, wire bonds, and box resonances. The simulated microwave cavity mode is not qualitatively affected by these limitations, but we should treat the optomechanical coupling it yields as an optimistic estimate.

We characterize our microwave resonator by recording its reflected response (both amplitude and phase) and fitting this

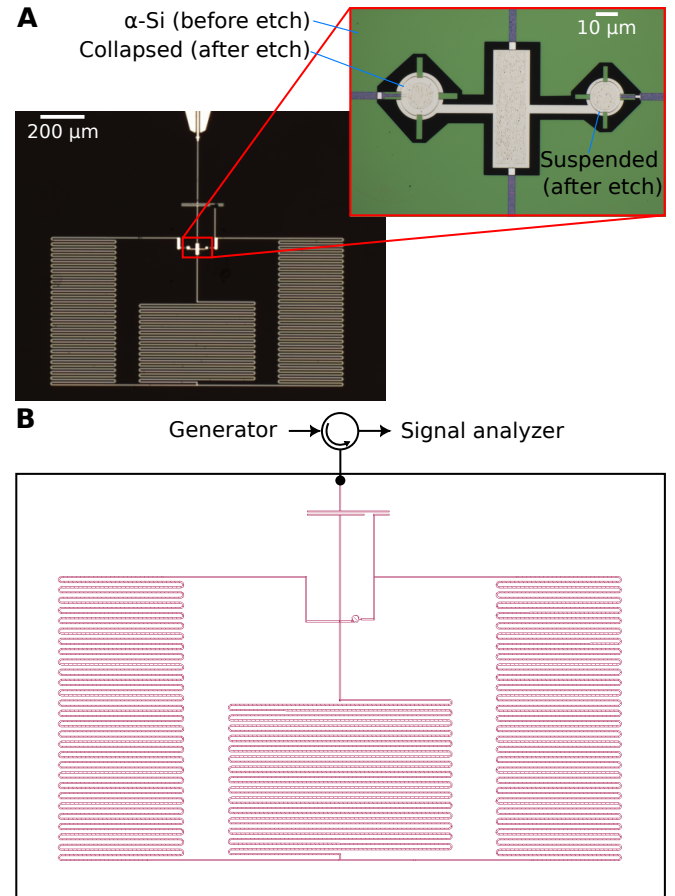


**Fig. S10 | Microwave cavity.** **A:** Microscope image of our microwave cavity (after the experiment), with the inset showing the drums (during fabrication). The larger (left) drum collapsed before the experiment, while the smaller (right) drum survived. **B:** Sonnet simulation of our cavity, with the collapsed drum replaced by a short.

with the equation<sup>48</sup>

$$R = \frac{(\kappa_i - \kappa_e)/2 - i(\Delta - \omega_c)}{(\kappa_i + \kappa_e)/2 - i(\Delta - \omega_c)}. \quad (\text{S11})$$

Here, the square of the reflection coefficient,  $|R|^2$ , describes the probability that a photon reflects off our cavity. Furthermore, the internal and external linewidths,  $\kappa_i$  and  $\kappa_e$ , sum up to the total linewidth  $\kappa = \kappa_i + \kappa_e$ , and the detuning  $\Delta = \omega_d - \omega_c$  describes the difference between the drive frequency  $\omega_d$  and the cavity center frequency  $\omega_c$ .

We use a three-step fit process. First, we de-trend the cavity signal by fitting a polynomial of order 2 to the first and last 10% of the amplitude signal, and a polynomial of order 1 to the same parts of the phase signal. This assumes the cavity resonance is approximately at the center of our measurement span, and that the background is reasonably flat within this span. Then we fit an ellipse to the response  $R$  on a Smith chart, from which we compute the cavity parameters and use those as initial guesses for the third and final step. By using scipy's `curve_fit` function<sup>61</sup>, we fit our data to Eq. (S11). The response, fit and extracted parameters are shown in Fig. S11.

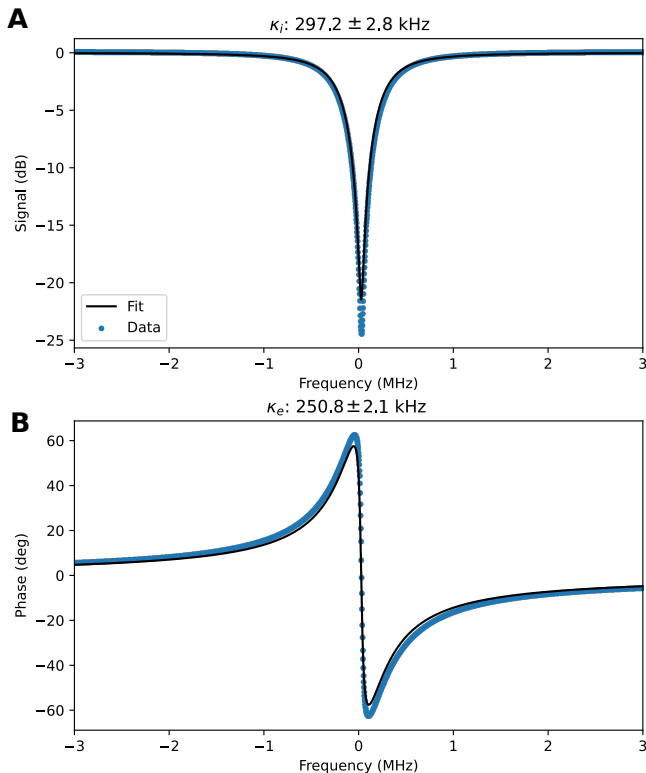


**Fig. S11 | Microwave cavity calibration.** **A:** Amplitude response of the microwave cavity (blue) and the fitted linewidth (black). **B:** Phase response of the microwave cavity (blue) and the fitted response (black). The internal and external linewidths,  $\kappa_i = 297.2 \pm 2.8$  kHz and  $\kappa_e = 250.8 \pm 2.1$  kHz respectively, are fitted as described in the text.

We fit the amplitude in logarithmic scale to enhance the accuracy around the cavity center, while the phase is fitted in linear scale.

Our cavity resonance frequency  $\omega_c = 2\pi \times 5.46180$  GHz, and the internal and external linewidths are  $\kappa_i = 2\pi \times 297.2 \pm 2.8$  kHz and  $\kappa_e = 2\pi \times 250.8 \pm 2.1$  kHz respectively.

## 2. Thermalization of drum motion

We calibrate the temperature to which the mode of our mechanical resonator thermalizes by sweeping the temperature of the dilution refrigerator. At each temperature, we measure the mechanical spectrum and fit a Lorentzian to the data. This way, we can extract the frequency  $\omega_m$ , linewidth  $\gamma_m$ , and the area of the mechanical peak.

The amplitude of the thermal motion peak is shown in Fig. S12. It increases linearly with temperature below 200 mK. At higher temperatures the quasiparticles in the Al superconducting cavity shift and damp the cavity mode which reduces the readout efficiency. The peak amplitude stays proportional to the temperature all the way to the base temperature of 10 mK: we conclude that the drum thermalizes down to 10 mK and we use this assumption to extract  $g_0$  in the next

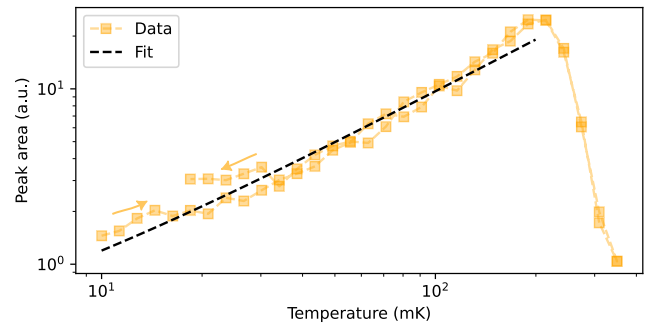


**Fig. S12 | Thermalization of the drum mode.** Area of the fitted mechanical peaks, indicating the thermal energy of the oscillator mode. The dashed curve is a linear fit offset by only about 3 mK, well below the base temperature of 10 mK, showing the good thermalization of the mode with the cryostat at the base temperature. At higher temperatures, the microwave cavity response disappears, likely due to quasiparticles in the superconductor (Aluminium), which shifts the microwave cavity frequency.

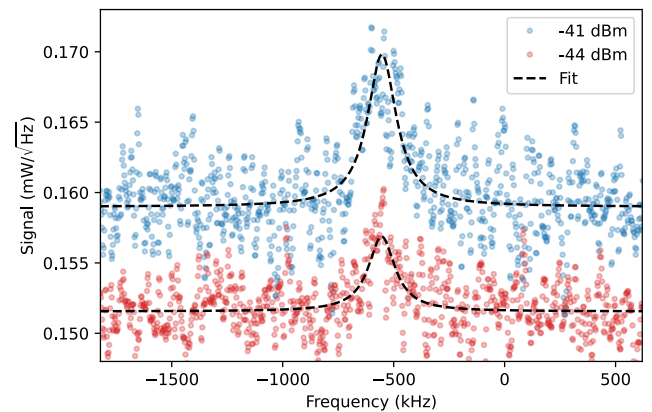


**Fig. S13 | Calibration of the optomechanical coupling rate.** The amplitude of the scattered peak is compared to a signal of known power (not shown). The area under the peak is calculated from a Lorentzian fit, and the ratio of the fitted peak with the signal of known power yields the optomechanical coupling rate  $g_0$ .

section.

## 3. Calibration of single-photon coupling

The optomechanical coupling  $g_0$  is calibrated by sending in a tone at the red sideband,  $\omega_c - \omega_m$ , and comparing the amplitude of the scattered peak with the amplitude of the drive. The resulting signal is shown in Fig. S13, and we fit a Lorentzian curve to the peak. We extract the area  $A$  under the curve, which is proportional to the number of scattered photons, and we compare it to the number of photons in the drive tone,  $\hat{a}_{sb}^\dagger \hat{a}_{sb}$ . The optomechanical coupling can be extracted from these amplitudes as

$$g_0^2 = \frac{A}{\hat{a}_{sb}^\dagger \hat{a}_{sb}} \frac{|1 - \kappa_e \chi(\omega_c - \omega_m)|^2 |\chi(\omega_c - \omega_m)|^2}{|\chi \omega_c|^2 n_m}, \quad (\text{S12})$$

which contains the ratio of the peak amplitude, as well as the cavity susceptibilities at the red sideband and cavity center (assuming zero detuning),

$$\begin{aligned}\chi(\omega_c - \omega_m) &= \frac{1}{\kappa/2 + i\omega_m} \\ \chi(\omega_c) &= \frac{1}{\kappa/2}.\end{aligned}\quad (\text{S13})$$

The thermal mechanical occupation can be calculated as

$$n_m = \frac{k_B T}{\hbar\omega_m}.\quad (\text{S14})$$

With these expressions, we fit  $g_0 = 2\pi \times 150 \pm 9$  Hz.

#### 4. Effective linewidth

We account for optical damping (sideband cooling) by using an effective linewidth,  $\gamma_{\text{eff}}$  that relates to the intrinsic (low-power) mechanical linewidth  $\gamma_m$  via

$$\gamma_{\text{eff}} = \gamma_m + \frac{4g_0^2|\alpha|^2}{\kappa}P = \gamma_m + \eta P.\quad (\text{S15})$$

Here,  $|\alpha|^2$  is the number of photons in the cavity at the red sideband frequency,  $\eta$  is some coefficient which we are trying to fit and  $P$  is the power sent out from our microwave source at the red sideband frequency. The exact value of  $\eta$  depends not only on optomechanical parameters  $g_0$  and  $\kappa$ , but also on the attenuation in the microwave lines between source and sample. However, as long as the latter are constant between measurements, we can use  $\eta$  and do not need to know the exact attenuation from our lines.

To fit the intrinsic linewidth, mechanical frequency and  $\eta$ , we vary the power sent in on the red sideband.

#### 5. Scale and phonon number calibration

We do not know a priori the exact scaling between the spectral power that we measure and the expected spectral power of a single photon or phonon. Thus we need to derive an expression for the spectral power in terms of system parameters that can be measured, to use it as a fit function to our measurements.

We start from the equations of motion for the cavity field  $\hat{a}$  and mechanical motion  $\hat{b}$ . In the sideband-resolved limit, with a drive  $\omega_m$  lower than the cavity frequency (at the red sideband), with  $\hat{a}$  separated into a steady state amplitude and some fluctuations  $\hat{a} = \alpha + \delta\hat{a}$ , the equations of motion can be written in the frequency domain as

$$\begin{aligned}\hat{a}[\omega] &= \chi_c[\omega + \Delta] \left( -ig_0\alpha \left( \hat{b}[\omega] + \hat{b}^\dagger[\omega + 2\omega_m] \right) + \sqrt{\kappa_i}\hat{a}_{\text{in}}[\omega] \right), \\ \hat{b}[\omega] &= \chi_m[\omega] \left( -ig_0 \left( \alpha^*\hat{a}[\omega] + \alpha\hat{a}^\dagger[\omega + 2\omega_m] \right) + \sqrt{\gamma_m}\hat{b}_{\text{in}}[\omega] \right).\end{aligned}\quad (\text{S16})$$

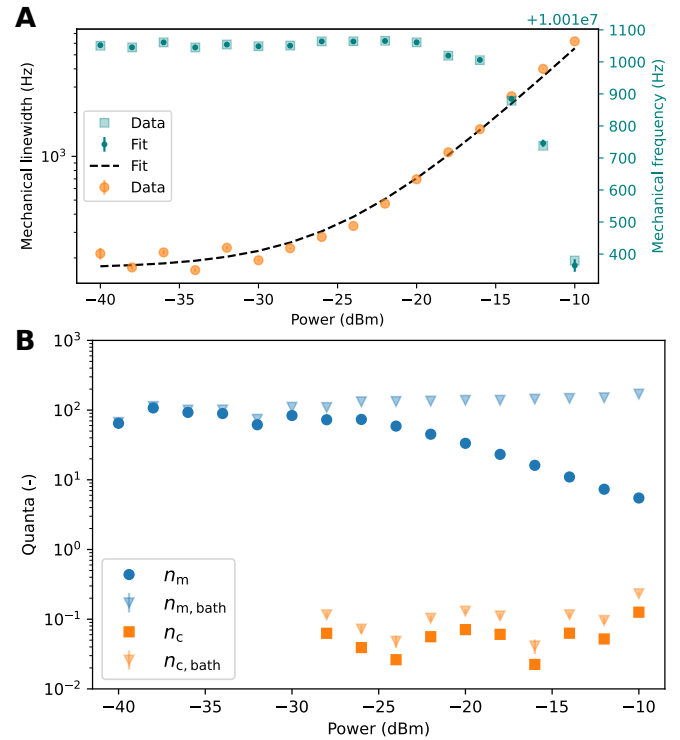


**Fig. S14 | Power calibration.** **A:** Mechanical linewidths (orange) and frequencies (teal) for various driving powers on the red sideband. **B:** Extracted mechanical occupation  $n_m$  and cavity photon number  $n_c$ , as well as the equivalent quanta in the respective thermal baths.

Here, the cavity susceptibility  $\chi_c[\omega] = \frac{1}{\kappa/2 - i\omega}$  and the mechanical susceptibility  $\chi_m[\omega] = \frac{1}{\gamma_m/2 - i\omega}$  are used as shorthands, and the input fields are  $\hat{a}_{\text{in}}[\omega]$  and  $\hat{b}_{\text{in}}[\omega]$ .

In the good cavity limit, we can neglect the terms at  $\omega \pm 2\omega_m$  and  $\Delta$ . We can replace  $\hat{b}[\omega]$  in our expression for  $\hat{a}[\omega]$  and compute the spectrum  $S_{\text{out}}$  of the output field  $\hat{a}_{\text{out}}[\omega] = \hat{a}_{\text{in}}[\omega] - \sqrt{\kappa_e}\hat{a}[\omega]$ . We get

$$S_{\text{out}} = \frac{1}{2} + \kappa_e\kappa_i |\tilde{\chi}_c[\omega]|^2 n_{\text{cav}} + g_0^2|\alpha|^2\gamma_m\kappa_e |\tilde{\chi}_c[\omega]\chi_m[\omega]|^2 n_{\text{th}}.\quad (\text{S17})$$

The three terms come from the external port of the cavity (vacuum), environmental noise at the cavity frequency ( $n_{\text{cav}}$ ) and mechanical noise (thermal,  $n_{\text{th}}$ ). The shorthand  $\tilde{\chi}_c[\omega] = \frac{\chi_c[\omega]}{1 + g_0^2|\alpha|^2\chi_c[\omega]\chi_m[\omega]}$  denotes the cavity susceptibility that is modified due to the optomechanical interaction. In the fitting procedure, we subtract the constant offset, so the factor 1/2 in Eq. (S17) disappears. Our final fit has the form  $S_{\text{fit}} = S_c \times (S_{\text{out}}[\omega] - 1/2)$ , and requires knowing  $\kappa_e, \kappa_i, \gamma_m, g_0, \alpha, n_{\text{cav}}$ , and  $n_{\text{th}}$  to extract our fit parameter, scale  $S_c$ . In favor of knowing  $\alpha$  directly, we can use  $g_0^2|\alpha|^2 = \frac{\kappa\eta P}{4}$  using the parameter  $\eta$  defined in Eq. (S15).

The fit procedure is as follows: We assume that at sufficiently low red-detuned drive power, the mechanical occupation is unperturbed by the drive. For the points at the lowest powers shown in Fig. S14A, below -32 dB,  $n_m$  is known from the reference temperature obtained from the thermalization step. Then we use the power-dependence parameter  $\eta$

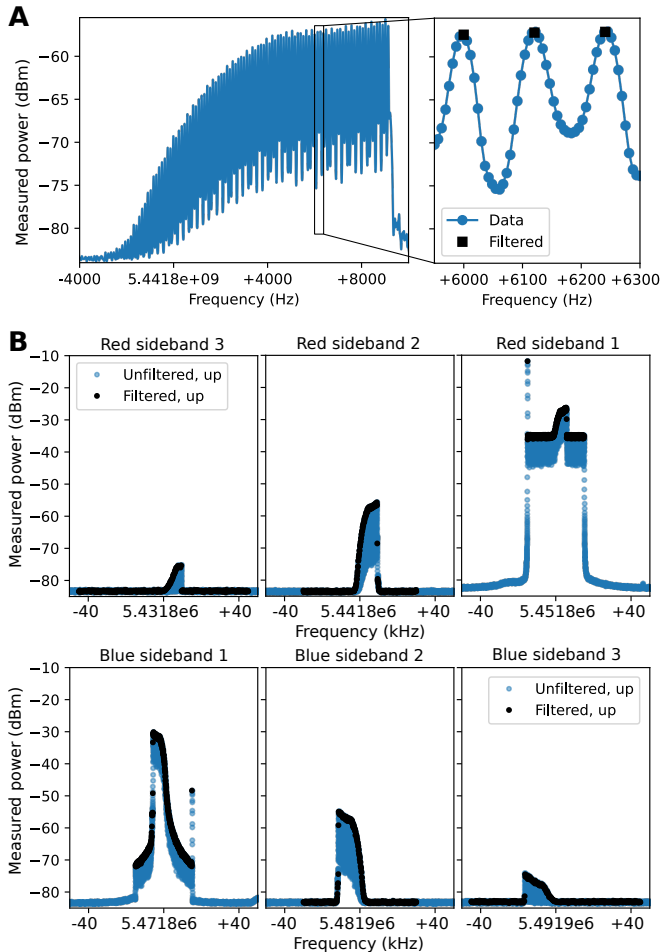


**Fig. S15 | Data filtering.** **A:** The measured power on the spectrum analyzer shows periodic peaks at the sideband drive frequency steps. We filter out the peaks located at these frequencies (black squares). **B:** All sidebands as recorded on the spectrum analyzer (blue) and filtered (black). Clearly visible is the noise pedestal due to the drive at the first red sideband. The sharp peak at the edge of the pedestal is from the vector network analyzer start/stop frequency.

obtained from the effective linewidth step, and fit the data at all powers to obtain  $n_m$  and  $n_c$  at each power. The effective linewidth is shown in Fig. S14A, with intrinsic mechanical linewidth  $\gamma_m = 168.9 \pm 9.5$  Hz and power factor  $\eta = 5.37 \cdot 10^4$  Hz mW<sup>-1</sup> completing the fit.

With our initial guess of the occupation numbers, we subsequently refine the fits of our scale parameter and  $\eta$  (now using the whole dataset). Using the updated values, we re-fit  $n_m$  and  $n_c$  at all powers, and the final result is shown in Fig. S14B. In the plots, we have used the final  $\eta = 5.37 \cdot 10^4$  Hz mW<sup>-1</sup>, and scale  $S_c = 2.04 \cdot 10^{-15} \frac{\text{W}/\sqrt{\text{Hz}}}{n_c}$ .

#### D. Data filtering

Due to limitations of our vector network analyzer, we drive our system at a series of discrete frequencies instead of a con-

tinuous sweep. This way, we can control the step size and direction, which allows us to do a bidirectional measurement where the drive frequency first increases and then decreases. We record the response of our system on a separate spectrum analyzer (SA), which integrates for the full duration of the increasing/decreasing segments separately. The response measured at the second red sideband ( $\omega_c - 2\omega_m$ ) during the upwards frequency sweep is shown in Fig. S15A.

Our SA records the spectrum using a much finer set of points than the frequencies at which the vector network analyzer outputs its drive. This condition creates a periodic pattern of peaks in the SA-recorded spectrum, which obscures the true shape of the curve. We are only interested in the tops of the peaks, since there is no sideband drive at the frequencies between the peaks. We filter the SA points in a small bandwidth around each of the vector network analyzer output frequencies, and integrate the power over that bandwidth. The filtered signal is a much shorter set of points that traces out the tops of the peaks. We have plotted the unfiltered data and the filtered signals as blue dots and black squares respectively in Fig. S15A.

#### E. Exclusion of other sources of nonlinearity

##### 1. Electrostatic nonlinearity: Average potential offset

The top and bottom plates of our drum form a capacitance separated by a vacuum gap at equilibrium of  $d' \simeq 15$  nm. Any static average potential difference between the plates exerts an attractive force between the plates, which has been used in a similar system to tune the vacuum gap<sup>30</sup>. In our system, the top and bottom plates are connected directly through the superconducting cavity, thus they are two sides of the same superconductor. In the absence of a large thermal gradient across our device, we expect the average potential difference between the plates to be negligibly small. Nonetheless, if there were a 1 V static average potential difference, this would correspond to a pressure of  $P_{\text{elec}} \simeq 150$  Pa for  $d' = 15$  nm (based on a COMSOL simulation, as shown in Fig. S16). This pressure is negligible compared to the Casimir pressure, which at this distance is  $P_c = 12.0 \pm 0.6$  kPa.

Our experiment is not directly sensitive to the absolute value of the (Casimir) pressure, and neither are we directly sensitive to any absolute pressure from the electrostatic force. We are sensitive to the *nonlinearity* that originates from these effects: The electrostatic force contributes a softening nonlinearity that scales with  $P_{\text{elec}} \propto d'^{-2}$ . This scaling is much weaker than the Casimir force scaling,  $P_c \propto d'^{-3.2}$ . Since the magnitude of the electrostatic force is much less and the nonlinearity scales much weaker than the Casimir force, the effect from the average potential difference is negligible.

##### 2. Electrostatic nonlinearity: Potential patches

It is well known that crystal grain orientations can cause local differences in the electrostatic potential<sup>62</sup>, also known

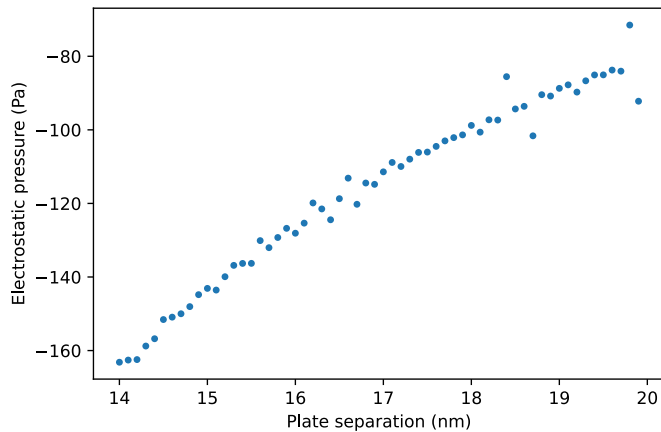


**Fig. S16 | Electrostatic effects.** Electrostatic pressure due to a 1 V static potential offset between the drum plates, as a function of their separation distance  $d$ . Due to the small energies involved and the geometry of the simulation, it is sensitive to mesh-related inaccuracies.

as potential patches<sup>63</sup>. This means that although two closely spaced conductors may have the same *average* potential, there may still be a non-zero attractive electrostatic force between the conductors. Numerical simulations of randomized patch geometries can be used to estimate the force contributed by these potential patches<sup>50,63,64</sup>. Such numerical simulations rely on accurate information about the (lateral) sizes of these patches, as well as their voltage distribution<sup>65,66</sup>.

We experimentally measure the patches in our aluminium to have a characteristic size of  $\ell = 158$  nm and a potential intensity that falls well within a normal distribution width  $\sigma = 100$  mV. With these numbers, we overestimate the pressure exerted by potential patches by about a factor 10. Nonetheless, we find that the patch pressure is several orders of magnitude smaller than the Casimir pressure at our equilibrium position  $d' = 15.1$  nm, as shown in Fig. S17. We exclude that potential patches are responsible for the nonlinearity that we observe in our mechanical resonator. We describe the experimental details in the next paragraphs.

#### *KPFM measurement of patches*

We use Kelvin Probe Force Microscopy (KPFM) to locally measure the potential on our sample, which is a well-established technique based on a conductive atomic force microscope cantilever<sup>67,68</sup>. We use a sample that was fabricated in the same batch as the sample reported in the main paper. The KPFM measurement results are plotted in Fig. S18, where we see characteristic aluminium spots where the potential is  $\approx 100$ – $200$  mV below the mean. This corresponds to the work function difference between the different crystalline orientations of aluminium: The work function of aluminium in the  $\langle 100 \rangle$ -direction is 4.20 eV, in the  $\langle 110 \rangle$ -direction it is 4.06 eV and in the  $\langle 111 \rangle$ -direction it is 4.26 eV<sup>69</sup>. There is no correlation between the potential and height, which are measured simultaneously.

#### *Patch intensity*

We expect a Gaussian distribution of the potentials, since the crystalline orientations should be random. But when we

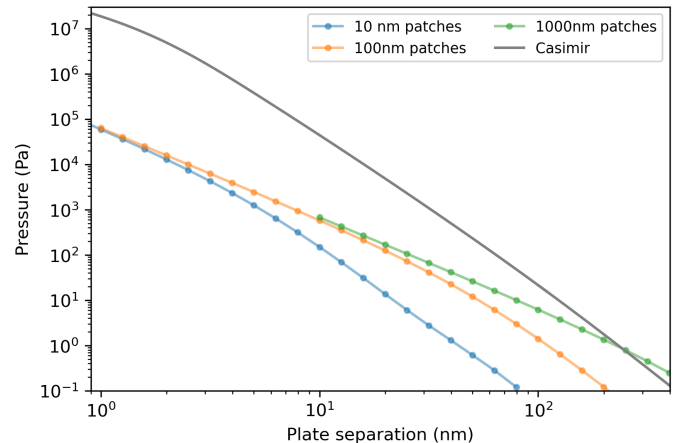


**Fig. S17 | Patch pressure.** Calculated Casimir pressure and patch potential pressure for patches normally distributed with a standard deviation of 100 mV, for various patch sizes.

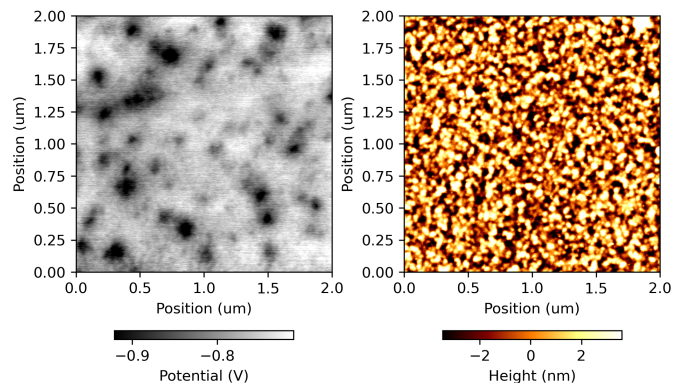


**Fig. S18 | Potential patches.** Measured surface potential (left) and height (right) of a  $2 \times 2 \mu\text{m}^2$  aluminium film from the same fabrication batch as the sample studied in the main text.

bin the measurement points of the potential, the Gaussian fit shown in Fig. S19 is not a good fit. There is a distinct tail towards lower potentials, which represents the spots seen in Fig. S18. The Gaussian fit is centered around a mean value  $-768$  mV with a standard deviation  $\sigma$  of 30.4 mV. The mean potential seen in Fig. S18 is due to being measured center conductor of the cavity, which is not directly connected to ground. Our KPFM tip touches down before the measurement and this transfers some charge to the sample. Any excess charge leaks out over time (timescale of approximately 30 minutes in air), so our measurement shows some offset potential.

#### *Patch size*

Besides the intensities of the potential patches, their spatial extent (average patch feature size  $\ell$ ) strongly affects the distance scaling of the electrostatic force they exert<sup>50,64</sup>. Recent simulations show that the lateral resolution of the KPFM probe can lead to an overestimation of the patch size and an underestimation of the patch intensity<sup>70</sup>. We use ASY-ELEC02 probes in our AFM, which have a nominal tip ra-

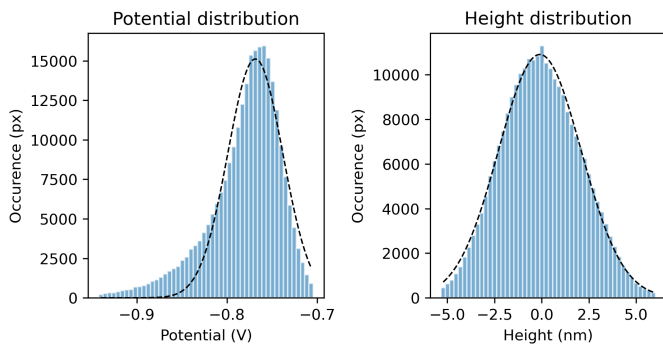


**Fig. S19 | Potential patch statistics.** Distribution of the measured potentials and heights for the area shown in Fig. S18, and Gaussian fits (dashed black lines).

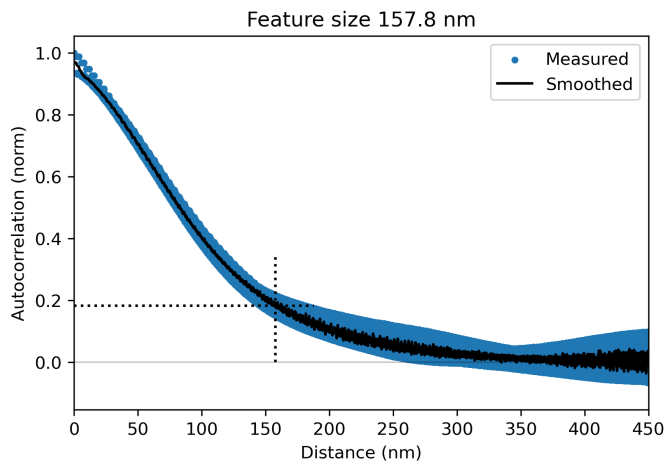


**Fig. S20 | Potential patch size.** Autocorrelation of the potential shown in Fig. S18. The average patch size  $\ell_p$  is the distance at which the normalized autocorrelation drops to  $1/2e \approx 0.184$  (dotted lines), which is 157.8 nm for our aluminium film.

dus of 25 nm, and operate in tapping mode with an amplitude 10 nm. With these numbers, we can estimate the lateral resolution of our KPFM measurement using<sup>71</sup>  $\ell_{\min} = \sqrt{RH} \approx 16$  nm where  $R$  is the tip radius and  $H$  is the minimal tip-sample distance. We determine the average size of the experimentally measured patches using the `correlate2d` function from Scipy, which is plotted in Fig. S20. We find the average patch size  $\ell_p$  is 158 nm, which is well above our minimal lateral resolution,  $\ell_p \gg \ell_{\min}$ . Thus there is no reason to assume we significantly overestimate the characteristic patch size  $\ell$  or underestimate the patch intensity distribution width  $\sigma$ . Our KPFM measurement also measures the height variation in our sample. The height is well-described by a Gaussian fit centered around  $-0.1$  nm with a  $\sigma_h$  of 2.19 nm and a characteristic feature size  $\ell_{\text{height}} = 32$  nm, as shown in Fig. S19.

#### Patch textures reproducibility

Our patch characterization was performed on a sample that was processed identically (i.e., in the same batch) as the sample in which we measured the Casimir force. We have measured the patch statistics on 8 separate areas on the aluminium

parts of the sample, and obtained similar patch intensities and patch sizes. The average patch intensity distribution width from all 8 areas  $\sigma_{\text{mean}} = 36$  mV, and the average patch size is  $\ell_{\text{mean}} = 160$  nm, with both parameters varying minimally between different measurement areas.

While some processing steps greatly affect the size and intensity of potential patches<sup>72</sup>, we have performed KPFM measurements on multiple samples (from different batches) and found our processing does not significantly affect the potential patches. The patch intensity does not appear affected by our release etch step, as we have measured  $\sigma_{\text{mean}} = 41$  mV before release ( $\sigma_{\text{mean}} = 36$  mV after). The heat treatment step has the largest effect on the patch intensity,  $\sigma_{\text{mean}} = 63$  mV before any heat treatment,  $\sigma_{\text{mean}} = 55$  mV after 15 minutes of 200 °C,  $\sigma_{\text{mean}} = 47$  mV after 15 minutes of 240 °C,  $\sigma_{\text{mean}} = 42$  mV after 15 minutes of 260 °C, and  $\sigma_{\text{mean}} = 41$  mV after 15 minutes of 280 °C. These findings appear consistent with potential patches that originate solely from the crystalline structure of the material. Our patch measurements were performed on a sample that has been processed simultaneously and identically to the experimentally reported sample, so we consider them to be representative of the patches present in the drum we tested.

#### Estimate of patch forces

We calculate the effect of patches for our drum geometry using the simulation framework we developed in an earlier work<sup>50</sup>. We generate Voronoi patterns based on randomized patches of various sizes, with normally distributed potentials with a  $\sigma = 100$  mV. Our patterns consist of 400 patches, and we compute the electrostatic energy. From the variation of energy with plate separation, we extract the pressure from the patch potentials for various plate separations as shown in Fig. S17. We find the well-known limit behaviors with the patch size<sup>63</sup>: When  $\ell \gg d$ ,  $P_{\text{patch}} \propto d^{-2}$ , while when  $\ell \ll d$ ,  $P_{\text{patch}} \propto d^{-4}$ . The regime where  $\ell \gg d$  leads to the greatest patch pressure in absolute sense, yet this is still several orders of magnitude smaller than the Casimir pressure for our plate separation  $d = 15$  nm. We find  $P_{\text{patch}} = 230$  Pa at a vacuum gap of 15 nm, much smaller than the Casimir pressure  $P_c = 12000 \pm 600$  Pa, as shown in Fig. S17. We note that in Casimir experiments at larger distances ( $d \gtrsim 200$  nm), the Casimir pressure can be comparable in amplitude to the patch pressure.

### 3. Mechanical nonlinearity: Geometric origin

There is a significant body of literature on the mechanical nonlinearities with a purely geometric origin. In our experimental platform of superconducting Aluminium drum resonators, Ref.<sup>73</sup> provides an excellent theoretical background that is experimentally tested in Ref.<sup>74</sup>. The nonlinearity due to geometry is a *hardening* nonlinearity in these drum resonators, both on theoretical grounds and experimental evidence<sup>73,74</sup>. The Casimir force contributes a *softening* nonlinearity, which is exactly what is described in the main text, and thus we exclude the geometric nonlinearity on qualitative grounds.

Furthermore, we can exclude the geometric mechanical

nonlinearity on quantitative grounds. We follow the method of Ref.<sup>73</sup>, which is based on Kirchoff-Love theory for circular membranes. The first assumption in this method is that the resonator is essentially a 2D circular membrane with coordinates  $(r, \theta)$ , which has modes purely moving in the out-of-plane  $z$  direction. From COMSOL simulations, we verify that the mode shown in Fig. 8B consists for  $> 99\%$  of motion in the  $z$ -direction. Thus we separate the variables of the function  $f_{n,m}$  describing the motion of our structure for the  $(n, m)$  mode,

$$f_{n,m}(r, \theta, t) = z_{n,m}(t)\psi_{n,m}(r, \theta). \quad (\text{S18})$$

The part  $z_{n,m}(t)$  describes the oscillating motion, and  $\psi_{n,m}(r, \theta)$  is the normalized mode shape. The mass and stiffness parameters of the fundamental mode (which is the one we study) are given as<sup>73</sup>

$$\begin{aligned} \mathcal{M}_{0,0} &= \rho h \int_0^{2\pi} \int_0^{R_d} (\psi_{0,0}(r, \theta))^2 r dr d\theta, \\ \mathcal{K}_{0,0} &= \frac{1}{12} \frac{Eh^3}{1 - \nu_r^2} \int_0^{2\pi} \int_0^{R_d} (\psi_{0,0}(r, \theta) \Delta^2 \psi_{0,0}(r, \theta)) r dr d\theta \\ &\quad + h\sigma_0 \int_0^{2\pi} \int_0^{R_d} (\psi_{0,0}(r, \theta) \Delta \psi_{0,0}(r, \theta)) r dr d\theta. \end{aligned} \quad (\text{S19})$$

We denote the material parameters:  $\rho$  is the density of the drum material,  $E$  is the Young's modulus,  $\nu_r$  the Poisson's ratio, and  $\sigma_0$  the stress (negative for tensile stress). The drum geometry is taken into account via the drum radius  $R_d$  and thickness  $h$ . Finally,

$$\Delta \dots = \frac{1}{r} \frac{\partial \dots}{\partial r} \left( r \frac{\partial \dots}{\partial r} \right) + \frac{1}{r^2} \frac{\partial^2 \dots}{\partial \theta^2} \quad (\text{S20})$$

is the Laplacian operator in polar coordinates. From Eq. (S19), we can calculate the mode frequency  $\omega_{0,0} = \sqrt{\mathcal{K}_{0,0}/\mathcal{M}_{0,0}}$ .

In the COMSOL model shown in Fig. 8, we use material parameters  $\rho = 2700 \text{ kg m}^{-3}$ ,  $E = 76.6 \text{ GPa}$ ,  $\nu_r = 0.32$ , and the average value of the von Mises stress over the drum domain,  $\sigma_0 = -270 \text{ MPa}$  (following the convention of Ref.<sup>73</sup>, tensile stress is negative in the analytical description, while in the COMSOL plots tensile stress is positive). Combined with the drum diameter  $2R_d = 11.3 \text{ }\mu\text{m}$  and the thickness of the evaporated Al  $h = 120 \text{ nm}$ , we can evaluate Eq. (S19). We find  $\mathcal{M}_{0,0} = 1.38 \times 10^{-13} \text{ kg m}^2$  and  $\mathcal{K}_{0,0} = 1467 \text{ N m}$ . The resulting frequency  $\omega_{0,0} = 2\pi \times 16.4 \text{ MHz}$  is close to our bare resonator frequency  $\omega_r = 2\pi \times 16.3 \text{ MHz}$ .

The geometric nonlinearity can be captured in a cubic term ( $\propto x^3$ ), and its coefficient for the fundamental mode can be found from the expression<sup>73</sup>

$$\tilde{\mathcal{K}}_{0,0} = -\frac{Eh}{R_d^2} \frac{C_{0,0}^{(1)}}{1 - \nu_r} \int_0^{2\pi} \int_0^{R_d} (\psi_{0,0}(r, \theta) \Delta \psi_{0,0}(r, \theta)) r dr d\theta \quad (\text{S21})$$

where  $C_{0,0}^{(1)} = 0.389664$  as tabulated in Table IV of Ref.<sup>73</sup>. From our COMSOL simulations, we obtain  $\tilde{\mathcal{K}}_{0,0} = 3.55 \times 10^{15} \text{ N m}^{-1}$ . We then relate this to the coefficient  $\alpha_D$  of the

Duffing term,

$$\ddot{x} + \gamma_r \dot{x} + \omega_r x + \alpha_D x^3 = \frac{F_d}{m_{\text{eff}}}, \quad (\text{S22})$$

where  $\alpha_D = \tilde{\mathcal{K}}_{0,0}/\mathcal{M}_{0,0} = +2.57 \times 10^{28} \text{ m}^{-2} \text{ s}^{-2}$ . This value is close to the experimental fit of Refs.<sup>73,74</sup>, which is  $\alpha_D = +7 \times 10^{27} \text{ m}^{-2} \text{ s}^{-2}$  in a drum resonator that is of nearly identical design to the one in this work.

From the coefficient  $\alpha_D$ , we can estimate that a +1 Hz frequency shift should occur if the motional amplitude is  $x \simeq 0.6 \text{ nm}$ . At those amplitudes, we see a multiple-kHz *negative* frequency shift corresponding to the Casimir force. Thus we can exclude the geometrical mechanical nonlinearity based on the magnitude and sign of the frequency shift.

#### 4. Nonlinear optomechanical coupling

The optomechanical cavity is formed by a plate capacitor where one of the plates is mechanically compliant. The coupling strength  $g_0$  is related to the shift in cavity frequency and to the capacitance  $C$  as<sup>48,74</sup>

$$\begin{aligned} g_0 &= -G x_{\text{zpf}} \\ G &= \frac{\partial \omega_c}{\partial x} = \frac{\partial \omega_c}{\partial C} \frac{\partial C}{\partial x}. \end{aligned} \quad (\text{S23})$$

The capacitance between two plates is not a linear function of their separation distance  $d$ , and  $g_0$  is typically based only on the first-order Taylor series of the capacitance in  $x/d$ . To estimate the 'higher order' optomechanical couplings that stem from the nonlinearity of the capacitance expansion, we follow the method of<sup>74</sup>. The cavity frequency and couplings up to third order in  $x$  are

$$\begin{aligned} \omega_c(x) &= \omega_c(0) - \left[ g_0 \frac{x}{x_{\text{zpf}}} + \frac{g_1}{2} \left( \frac{x}{x_{\text{zpf}}} \right)^2 + \frac{g_2}{2} \left( \frac{x}{x_{\text{zpf}}} \right)^3 \right] \\ g_1 &= g_0 \left[ 2 \frac{x_{\text{zpf}}}{d} - 3 \frac{g_0}{\omega_c(0)} \right] \\ g_2 &= g_0 \left[ 2 \left( \frac{x_{\text{zpf}}}{d} \right)^2 - 6 \frac{x_{\text{zpf}}}{d} \frac{g_0}{\omega_c(0)} + 5 \left( \frac{g_0}{\omega_c(0)} \right)^2 \right] \end{aligned} \quad (\text{S24})$$

For the parameters of our system, we evaluate  $g_0 = 2\pi \times 150 \text{ Hz}$ ,  $g_1 = 2\pi \times 6.4 \times 10^{-5} \text{ Hz}$  and  $g_2 = 2\pi \times 1.4 \times 10^{-11} \text{ Hz}$ . For a motion amplitude of  $x = 1 \text{ nm}$ , which is much larger than anything we observe, the linear frequency shift (only  $g_0$ ) is  $\Delta\omega_c = -32.58 \text{ MHz}$ , the quadratic shift (both  $g_0$  and  $g_1$ ) would be  $\Delta\omega_c = -34.10 \text{ MHz}$  and the cubic shift ( $g_0$ ,  $g_1$ , and  $g_2$ ) would be  $\Delta\omega_c = -34.17 \text{ MHz}$ . These higher-order capacitance contributions are only a relevant contribution to the frequency shift for extremely large displacements ( $\simeq \text{nm}$ ). At these displacements, the frequency shift is much larger than the cavity linewidth,  $\Delta\omega_c \gg \kappa$ , so the drive efficiency that we describe in the main text is the most important optomechanical effect to take into account. We emphasize that the nonlinearity from the plate capacitor expansion only affects the *cavity* frequency shift and not the mechanical frequency shift from the Casimir force.

| Quantity                        | Symbol                      | Value                                  |
|---------------------------------|-----------------------------|--|
| Unperturbed frequency           | $\omega_f$                  | $2\pi \times 16.710$ MHz               |
| Mechanical frequency            | $\omega_m$                  | $2\pi \times 13.688$ MHz               |
| Mechanical linewidth            | $\gamma_r \approx \gamma_m$ | $2\pi \times 231 \pm 4$ Hz             |
| Cavity frequency                | $\omega_c$                  | $2\pi \times 7.589718$ GHz             |
| External linewidth              | $\kappa_e$                  | $2\pi \times 304.7 \pm 2.8$ kHz        |
| Internal linewidth              | $\kappa_i$                  | $2\pi \times 608.7 \pm 6.2$ kHz        |
| Optomechanical coupling         | $g_0$                       | $2\pi \times 67 \pm 3$ Hz              |
| Effective mass                  | $m_{\text{eff}}$            | $3.96 \times 10^{-14}$ kg              |
| Rest separation without Cas. f. | $d$                         | $19.1 \pm 0.5$ nm                      |
| Rest separation                 | $d'$                        | $17.3 \pm 0.5$ nm                      |
| Bottom plate diameter           | $2r$                        | $11.3$ $\mu\text{m}$                   |
| Casimir amplitude               | $P$                         | $(1275 \pm 7) \cdot 10^{-24}$ Pa $m^2$ |
| Casimir force scaling exponent  | $n$                         | 3.193                                  |

**Table 2 | Parameters of the second device.**

### F. Measurements on a second device

We have repeated the experiments of the main text in a second device, fabricated using an identical design but in a

different fabrication run. The parameters of the device were characterized using the same method as for the device in the main text, and they are reported in Table 2. In the absence of the Casimir force, the devices have a similar mechanical resonance frequency. However, this second device has a slightly different separation of the plates at mechanical zero ( $d$ ), the final mechanical frequency is rather different due to the non-linear nature of the Casimir force. Due to the lower optomechanical coupling rate, and higher cavity linewidth, it requires more drive power to reach larger displacement amplitudes, and we are limited by the maximum power that our measurement chain can handle. These measurements were performed in a different dilution refrigerator to the experiments in the main text, with a separate set of measurement equipment.

One of the mechanical response curves of the second device is shown in Fig. S21. We have performed the same calibration procedure as in the device of the main text, and extract  $d = 19.1 \pm 0.5$  nm (solid black line) from a fit to the data. For completeness, we also show the theory curves for  $d = 19.6$  nm (dotted black line) and  $d = 18.6$  nm (dashed black line).

- [1] H. B. G. Casimir, On the attraction between two perfectly conducting plates, *Proc. Kon. Ned. Akad. v. Wet.* **51**, 793 (1948).
- [2] E. M. Lifshitz, The theory of molecular attractive forces between solids, *Journal of Experimental and Theoretical Physics* **2**, 73 (1956).
- [3] S. K. Lamoreaux, Demonstration of the Casimir force in the 0.6 to 6  $\mu\text{m}$  range, *Physical Review Letters* **78**, 5 (1997).
- [4] U. Mohideen and A. Roy, Precision measurement of the Casimir force from 0.1 to 0.9  $\mu\text{m}$ , *Physical Review Letters* **81**, 4549 (1998).
- [5] A. W. Rodriguez, F. Capasso, and S. G. Johnson, The Casimir effect in microstructured geometries, *Nature Photonics* **5**, 211 (2011).
- [6] L. M. Woods, D. A. R. Dalvit, A. Tkatchenko, P. Rodriguez-Lopez, A. W. Rodriguez, and R. Podgornik, Materials perspective on Casimir and van der Waals interactions, *Reviews of Modern Physics* **88**, 045003 (2016).
- [7] T. Gong, M. R. Corrado, A. R. Mahbud, C. Shelden, and J. N. Munday, Recent progress in engineering the Casimir effect - applications to nanophotonics, nanomechanics and chemistry, *Nanophotonics* **10**, 523 (2021).
- [8] F. M. Serry, D. Walliser, and G. J. Maclay, The role of the Casimir effect in the static deflection and stiction of membrane strips in microelectromechanical systems (MEMS), *Journal of Applied Physics* **84**, 2501 (1998).
- [9] H. B. Chan, V. A. Aksyuk, R. N. Kleiman, D. J. Bishop, and F. Capasso, Nonlinear micromechanical Casimir oscillator, *Physical Review Letters* **87**, 211801 (2001).
- [10] W. Broer, G. Palasantzas, J. Knoester, and V. B. Svetovoy, Significance of the Casimir force and surface roughness for actuation dynamics of MEMS, *Physical Review B* **87**, 125413 (2013).
- [11] L. Tang, M. Wang, C. Y. Ng, M. Nikolic, C. T. Chan, A. W. Rodriguez, and H. B. Chan, Measurement of non-monotonic Casimir forces between silicon nanostructures, *Nature Photonics* **11**, 97 (2017).
- [12] A. Stange, M. Imboden, J. Javor, L. K. Barrett, and D. J.

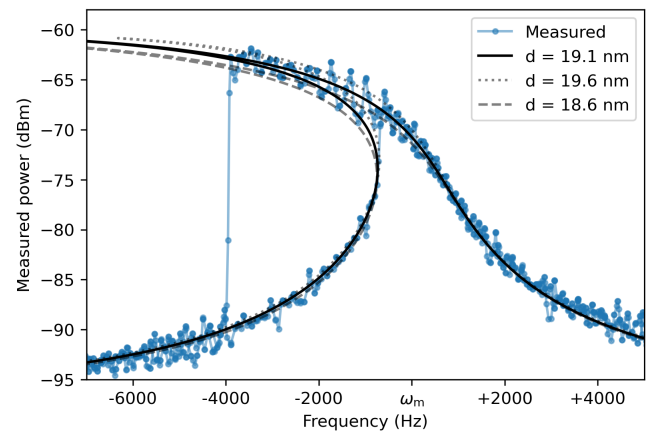


**Fig. S21 | Measurement of the Casimir nonlinearity in a second device.** The measured Casimir curve (blue) for 10 dBm cavity drive power and 0 dBm red sideband drive power. The theory curves based on the Casimir force for a separation of mechanical zero of  $d = 19.1$  nm (solid black line),  $d = 19.6$  nm (dotted black line) and  $d = 18.6$  nm (dashed black line) are overlaid on the measured data. The  $d = 19.1$  nm curve is closest to the center of the measured data.

- [13] J. M. Pate, M. Goryachev, R. Y. Chiao, J. E. Sharping, and M. E. Tobar, Casimir spring and dilution in macroscopic cavity optomechanics, *Nature Physics* **16**, 1117 (2020).
- [14] K. Y. Fong, H.-K. Li, R. Zhao, S. Yang, Y. Wang, and X. Zhang, Phonon heat transfer across a vacuum through quantum fluctuations, *Nature* **576**, 243 (2019).
- [15] Z. Xu, X. Gao, J. Bang, Z. Jacob, and T. Li, Non-reciprocal energy transfer through the Casimir effect, *Nature Nanotech-*

- nology **17**, 148 (2022).
- [16] V. B. Bezerra, G. L. Klimchitskaya, V. M. Mostepanenko, and C. Romero, Violation of the Nernst heat theorem in the theory of the thermal Casimir force between Drude metals, *Physical Review A* **69**, 022119 (2004).
- [17] J. S. Høyve, I. Brevik, S. A. Ellingsen, and J. B. Aarseth, Analytical and numerical verification of the Nernst theorem for metals, *Physical Review E* **75**, 051127 (2007).
- [18] A. O. Sushkov, W. J. Kim, D. A. R. Dalvit, and S. K. Lamoreaux, Observation of the thermal Casimir force, *Nature Physics* **7**, 230 (2011).
- [19] V. M. Mostepanenko, Casimir puzzle and Casimir conundrum: Discovery and search for resolution, *Universe* **7**, 84 (2021).
- [20] R. S. Decca, E. Fischbach, G. L. Klimchitskaya, D. E. Krause, D. López, and V. M. Mostepanenko, Improved tests of extra-dimensional physics and thermal quantum field theory from new Casimir force measurements, *Physical Review D* **68**, 116003 (2003).
- [21] G. L. Klimchitskaya, U. Mohideen, and V. M. Mostepanenko, Constraints on non-Newtonian gravity and light elementary particles from measurements of the Casimir force by means of a dynamic atomic force microscope, *Physical Review D* **86**, 065025 (2012).
- [22] U. Leonhardt, Lifshitz theory of the cosmological constant, *Annals of Physics* **411**, 167973 (2019).
- [23] G. Bimonte, E. Calloni, G. Esposito, and L. Rosa, Variations of Casimir energy from a superconducting transition, *Nuclear Physics B* **726**, 441 (2005).
- [24] D. Pérez-Morelo, A. Stange, R. W. Lally, L. K. Barrett, M. Imboden, A. Som, D. K. Campbell, V. A. Aksyuk, and D. J. Bishop, A system for probing Casimir energy corrections to the condensation energy, *Microsystems and Nanoengineering* **6**, 115 (2020).
- [25] G. Bimonte, H. Haakh, C. Henkel, and F. Intravala, Optical BCS conductivity at imaginary frequencies and dispersion energies of superconductors, *Journal of Physics A: Mathematical and Theoretical* **43**, 145304 (2010).
- [26] R. A. Norte, M. Forsch, A. Wallucks, I. Marinković, and S. Gröblacher, Platform for measurements of the Casimir force between two superconductors, *Physical Review Letters* **121**, 030405 (2018).
- [27] J. R. Rodrigues, A. Gusso, F. S. S. Rosa, and V. R. Almeida, Rigorous analysis of Casimir and van der Waals forces on a silicon nano-optomechanical device actuated by optical forces, *Nanoscale* **10**, 3945 (2018).
- [28] G. Bimonte, Casimir effect between superconductors, *Physical Review A* **99**, 052507 (2019).
- [29] R. S. Decca, D. López, E. Fischbach, G. L. Klimchitskaya, D. E. Krause, and V. M. Mostepanenko, Tests of new physics from precise measurements of the Casimir pressure between two gold-coated plates, *Physical Review D* **75**, 077101 (2007).
- [30] R. W. Andrews, A. P. Reed, K. Cicak, J. D. Teufel, and K. W. Lehnert, Quantum-enabled temporal and spectral mode conversion of microwave signals, *Nature Communications* **6**, 10021 (2015).
- [31] F. M. Serry, D. Walliser, and G. J. Maclay, The anharmonic Casimir oscillator (ACO) - The Casimir effect in a model microelectromechanical system, *Journal of Microelectromechanical Systems* **4**, 193 (1995).
- [32] H. B. Chan, V. A. Aksyuk, R. N. Kleiman, D. J. Bishop, and F. Capasso, Quantum mechanical actuation of microelectromechanical systems by the Casimir force, *Science* **291**, 1941 (2001).
- [33] J. D. Teufel, T. Donner, D. Li, J. W. Harlow, M. S. Allman, K. Cicak, A. J. Sirois, J. D. Whittaker, K. W. Lehnert, and R. W. Simmonds, Sideband cooling of micromechanical motion to the quantum ground state, *Nature* **475**, 359 (2011).
- [34] E. E. Wollmann, C. U. Lei, A. J. Weinstein, J. Suh, A. Kronwald, F. Marquardt, A. A. Clerk, and K. C. Schwab, Quantum squeezing of motion in a mechanical resonator, *Science* **349**, 952 (2015).
- [35] J.-M. Pirkkalainen, E. Damskägg, M. Brandt, F. Massel, and M. A. Sillanpää, Squeezing of quantum noise of motion in a micromechanical resonator, *Physical Review Letters* **115**, 243601 (2015).
- [36] F. Lecocq, J. B. Clark, R. W. Simmonds, J. Aumentado, and J. D. Teufel, Quantum nondemolition measurement of a nonclassical state of a massive object, *Physical Review X* **5**, 041037 (2015).
- [37] C. F. Ockeloen-Korppi, E. Damskägg, J.-M. Pirkkalainen, M. Asjad, A. A. Clerk, F. Massel, M. J. Woolley, and M. A. Sillanpää, Stabilized entanglement of massive mechanical oscillators, *Nature* **556**, 478 (2018).
- [38] S. Kotler, G. A. Peterson, E. Shojaei, F. Lecocq, K. Cicak, A. Kwiatkowski, S. Geller, S. Glancy, E. Knill, R. W. Simmonds, J. Aumentado, and J. D. Teufel, Direct observation of deterministic macroscopic entanglement, *Science* **372**, 622 (2021).
- [39] L. Mercier de Lépinay, C. F. Ockeloen-Korppi, M. J. Woolley, and M. A. Sillanpää, Quantummechanics-free subsystem with mechanical oscillators, *Science* **372**, 625 (2021).
- [40] R. Riedinger, S. Hong, R. A. Norte, J. A. Slater, J. Shang, A. G. Krause, V. Anant, M. Aspelmeyer, and S. Gröblacher, Nonclassical correlations between single photons and phonons from a mechanical oscillator, *Nature* **530**, 313 (2016).
- [41] I. Galinskiy, G. Enzian, M. Parniak, and E. S. Polzik, Nonclassical correlations between photons and phonons of center-of-mass motion of a mechanical oscillator, *Physical Review Letters* **133**, 173605 (2024).
- [42] A. D. O'Connell, M. Hofheinz, M. Ansmann, R. C. Bialczak, M. Lenander, E. Lucero, M. Neeley, D. Sank, H. Wang, M. Weides, J. Wenner, J. M. Martinis, and A. N. Cleland, Quantum ground state and single-phonon control of a mechanical resonator, *Nature* **464**, 697 (2010).
- [43] Y. Chu, P. Kharel, T. Yoon, L. Frunzio, P. T. Rakich, and R. J. Schoelkopf, Creation and control of multi-phonon Fock states in a bulk acoustic-wave resonator, *Nature* **563**, 666 (2018).
- [44] S. Marti, U. von Lüpkke, O. Joshi, Y. Yang, M. Bild, A. Oshen, Y. Chu, and M. Fadel, Quantum squeezing in a nonlinear mechanical oscillator, *Nature Physics* **20**, 1448 (2024).
- [45] Y. Yang, I. Kladarić, M. Drimmer, U. von Lüpkke, D. Lenterman, J. Bus, S. Marti, M. Fadel, and Y. Chu, A mechanical qubit, *Science* **386**, 783 (2024).
- [46] C. Samanta, S. L. De Bonis, C. B. Møller, R. Tormo-Queralt, W. Yang, C. Urgell, B. Stamenic, B. Thibeault, Y. Jin, D. A. Czaplowski, F. Pistolei, and A. Bachtold, Nonlinear nanomechanical resonators approaching the quantum ground state, *Nature Physics* **19**, 1340 (2023).
- [47] H. J. Eerikens, *Investigations of radiation pressure: Optical side-band cooling of a trampoline resonator and the effect of superconductivity on the Casimir force*, phdthesis, Universiteit Leiden (2017), ISBN: 9789085933243, <https://hdl.handle.net/1887/59506>.
- [48] M. Aspelmeyer, T. J. Kippenberg, and F. Marquardt, Cavity optomechanics, *Reviews of Modern Physics* **86**, 1391 (2014).
- [49] T. J. Kippenberg and K. J. Vahala, Cavity optomechanics, *Optics Express* **15**, 17172 (2007).
- [50] M. H. J. de Jong and L. Mercier de Lépinay, Simulating the

- electrostatic patch force in sphere-plate and plate-plate geometries, <https://arxiv.org/abs/2408.16323> (2024), arxiv preprint.
- [51] M. A. Sillanpää, R. Khan, T. T. Heikkilä, and P. J. Hakonen, Macroscopic quantum tunneling in nanoelectromechanical systems, *Physical Review B* **84**, 195433 (2011).
- [52] F. Pistolesi, A. N. Cleland, and A. Bachtold, Proposal for nanomechanical qubit, *Physical Review X* **11**, 031027 (2021).
- [53] M. Tinkham, *Introduction to superconductivity* (McGraw-Hill, Inc., 1996).
- [54] E. D. Palik, ed., *Handbook of optical constants of solids*, Vol. 1 (Academic, New York, 1997).
- [55] T. H. K. Barron, J. F. Collins, T. W. Smith, and G. K. White, Thermal expansion, Grüneisen functions and static lattice properties of quartz, *Journal of Physics C: Solid State Physics* **15**, 4311 (1982).
- [56] M. Pinard, Y. Hadjar, and A. Heidmann, Effective mass in quantum effects of radiation pressure, *European Physical Journal D* **7**, 107 (1999).
- [57] A. Dhooge, W. Govaerts, and Y. A. Kuznetsov, MATCONT: a MATLAB package for numerical bifurcation analysis of ODEs, *ACM Transactions on Mathematical Software* **29**, 141 (2003).
- [58] A. Dhooge, W. Govaerts, Y. A. Kuznetsov, H. G. E. Meijer, and B. Sautois, New features of the software MATCONT for bifurcation analysis of dynamical systems, *Mathematical and Computer Modelling of Dynamical Systems* **14**, 79 (2008).
- [59] M. Xu, R. J. G. Elbertse, A. Keşkekler, G. Bimonte, J. Lee, S. Otte, and R. A. Norte, Measuring Casimir force across a superconducting transition, <https://arxiv.org/abs/2504.10579> (2025), arxiv preprint.
- [60] B. He, Q. Lin, M. Orszag, and M. Xiao, Mechanical oscillations frozen on discrete levels by two optical driving fields, *Physical Review A* **102**, 011503 (2020).
- [61] P. Virtanen, R. Gommers, T. E. Oliphant, M. Haberland, T. Reddy, D. Cournapeau, E. Burovski, P. Peterson, W. Weckesser, J. Bright, S. J. van der Walt, M. Brett, J. Wilson, K. Jarrod Millman, N. Mayorov, A. R. J. Nelson, E. Jones, R. Kern, E. Larson, C. J. Carey, I. Polat, Y. Feng, E. W. Moore, J. VanderPlas, D. Laxalde, J. Perktold, R. Cimrman, I. Hendriksen, E. A. Quintero, C. R. Harris, A. M. Archibald, A. H. Ribeiro, F. Pedregosa, P. van Mulbregt, and Scipy 1.0 Contributors, Scipy 1.0: fundamental algorithms for scientific computing in Python, *Nature Methods* **17**, 261 (2020).
- [62] J. B. Camp, T. W. Darling, and R. E. Brown, Macroscopic variations of surface potentials of conductors, *Journal of Applied Physics* **69**, 7126 (1991).
- [63] C. C. Speake and C. Trenkel, Forces between superconducting surfaces due to spatial variations of surface potential, *Physical Review Letters* **90**, 160403 (2003).
- [64] J. Ke, W.-C. Dong, S.-H. Huang, Y.-J. Tan, W.-H. Tan, S.-Q. Yang, C.-G. Shao, and J. Luo, Electrostatic effect due to patch potentials between closely spaced surfaces, *Physical Review D* **107**, 065009 (2023).
- [65] R. O. Behunin, F. Intravaia, D. A. R. Dalvit, P. A. Maia Neto, and S. Reynaud, Modeling electrostatic patch effects in Casimir force measurements, *Physical Review A* **85**, 012504 (2012).
- [66] R. O. Behunin, Y. Zeng, D. A. R. Dalvit, and S. Reynaud, Electrostatic patch effects in Casimir-force experiments performed in sphere-plane geometry, *Physical Review A* **86**, 052509 (2012).
- [67] R. O. Behunin, D. A. R. Dalvit, R. S. Decca, and C. C. Speake, Limits on the accuracy of force sensing at short separations due to patch potentials, *Physical Review D* **89**, 051301 (2014).
- [68] J. L. Garrett, D. Somers, and J. N. Munday, The effect of patch potentials in Casimir force measurements determined by heterodyne Kelvin probe force microscopy, *Journal of Physics: Condensed Matter* **27**, 214012 (2015).
- [69] W. M. Haynes, ed., *CRC Handbook of Chemistry and Physics*, 96th ed. (CRC Press, Boca Raton, 2015).
- [70] K. Shi, P. Luo, J. Liu, H. Yin, and Z. Zhou, Dependence of electrostatic patch force evaluation on the lateral resolution of Kelvin probe force microscopy, <https://arxiv.org/abs/2411.01733> (2024), arxiv preprint.
- [71] G. Lévêque, P. Cadet, and A. Arinero, Sensitivity and resolution in noncontact electrostatic force microscopy in the case of a constant potential, *Physical Review B* **71**, 205419 (2005).
- [72] J. L. Garrett, J. Kim, and J. N. Munday, Measuring the effect of electrostatic patch potentials in Casimir force experiments, *Physical Review Research* **2**, 023355 (2020).
- [73] D. Cattiaux, S. Kumar, X. Zhou, A. Fefferman, and E. Collin, Geometrical nonlinearity of circular plates and membranes: An alternative method, *Journal of Applied Physics* **128**, 104501 (2020).
- [74] D. Cattiaux, X. Zhou, S. Kumar, I. Golokolenov, R. R. Gazizulin, A. Luck, L. Mercier de Lépinay, M. Sillanpää, A. D. Armour, A. Fefferman, and E. Collin, Beyond linear coupling in microwave optomechanics, *Physical Review Research* **2**, 033480 (2020).